Synthesis and Characterization of Eu doped M-type Barium Hexaferrites

By:

Anum Zafar

(317-FBAS/MSPHY/F14)

Supervisor:

Dr. Shafqat Karim

Head Nanomaterials Research Group

PINSTECH, Pakistan

Co-Supervisor:

Dr. Shaista Shahzada

Assistant Professor, Dept. of Physics, IIUI

Department of Physics
Faculty of Basic and Applied Sciences
International Islamic University, Islamabad

(2016)

MS
530
ANS

Magnetic properties.

Hysteresis curve.

Schematic representation.

International Islamic University, Islamabad
Faculty of Basic and Applied Sciences
Department of Physics

Synthesis and Characterization of Eu doped M-type Barium Hexaferrites

By

Anum Zafar

(317/FBAS/MSPHY/F-14)

Thesis submitted to

Department of Physics, IIUI

for the award of the degree of

MS Physics

Dr. Shamaila Sajjad
Chairperson
Department of Physics (FC. FBAS)
International Islamic University
Islamabad

Signature:_____

(Acting *Chairperson, Department of* Physics)

M. Azhar

Signature:_____

(Dean FBAS, IIU, Islamabad)

Dated: 09-02-2017

Final Approval

It is certified that the work presented in this thesis entitled "**Synthesis and characterization of Eu doped M-type Barium Hexaferrites**" by **Anum Zafar**, Registration No. **317-FBAS/MSPHY/F14** is of sufficient standard in scope and quality for the award of degree of MS Physics from International Islamic University, Islamabad.

Committee

External Examiner:

Dr. Iftikhar Hussain Gul,

School of Chemical and Materials Engineering,

National University of Science and Technology,

Islamabad

Internal Examiner

Dr. Wiqar Hussain Shah

Assistant Professor

Department of Physics

International Islamic University, Islamabad

Supervisor

Dr. Shafqat Karim

Head Nanomaterials Research Group

Physics Division

PINSTECH, Islamabad

Co-Supervisor

Dr. Shaista Shahzada

Assistant Professor, Department of Physics,

International Islamic University Islamabad

This thesis is submitted to the Faculty of Basic and Applied Sciences (FBAS), International Islamic University Islamabad (IIUI) in partial fulfillment of the requirement for the degree of MS Physics

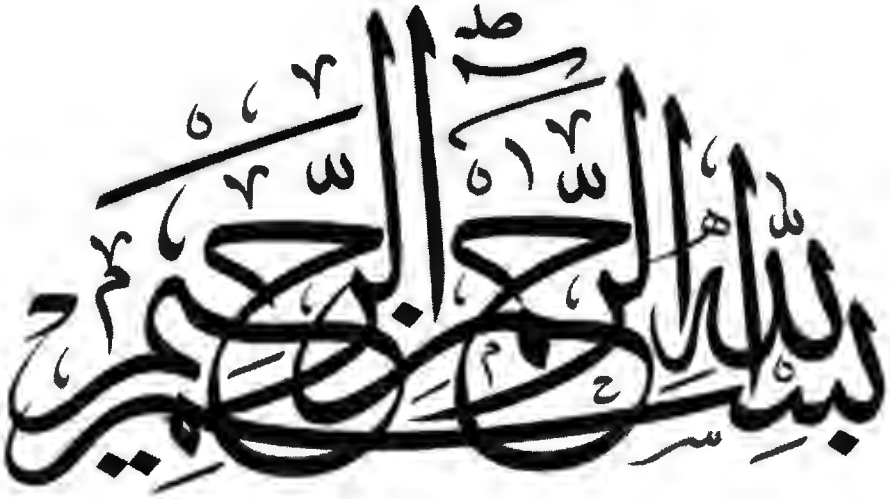
بسم الله الرحمن الرحيم

Declaration of Originality

I hereby declare that the work contained in this thesis and the intellectual content of this thesis are the product of our own work. This thesis has not been previously published in any form nor does it contain any material of the published resources which could be treated as infringement of the international copyright law.

I also declare that I do understand the terms of copyright and plagiarism and that in case of any copyright violation or plagiarism found in this work, I will be held fully responsible of the consequences of any such violation.

Anum Zafar

317/FBAS/MSPHY/F-14

Certificate

This is to certify that the work contained in this thesis entitled **"Synthesis and characterization of Eu doped M-type barium hexaferrites"** has been carried out by **Anum Zafar** in Pakistan Institute of Nuclear Science and Technology (PINSTECH) under the supervision of **Dr. Shafqat Karim**. In my opinion, this is fully adequate in scope and quality for the degree of MS Physics.

Supervisor

Dr. Shafqat Karim

Head Nanomaterials Research Group
Physics Division
PINSTECH, Islamabad

Co-Supervisor

Dr. Shaista Shahzada

Department of Physics
International Islamic University, Islamabad

Dedication

This thesis is dedicated to my beloved

Grandmother (late)

And my Parents

Table of Contents

Table of figures

List of tables

Acknowledgements

Praise is to the One, the Almighty, the merciful and the beneficent Allah, who is the source of all knowledge and wisdom, taught us what we knew not. We offer our humblest thank to the holy Prophet (Peace be upon him) who is forever a model of guidance and knowledge for humanity.

I would like to express my gratitude to my supervisor Dr Shafqat Karim for their inspiring guidance, remarkable suggestions, constant encouragement and co-operation during my project work. His guidance helped me in all the time of research and writing of thesis. I gratefully acknowledge for their technical support during my thesis project. I am also thankful to my Co-supervisor Dr. Shaista Shahzada for her advice and comments throughout my studies. I would like to express my sincere thanks to Dr. Ghafar Ali, Dr. Amjad Nisar and Dr. Mashkoor Ahmed for their collaboration, advice and valuable suggestions particularly in the method of conducting research. I am also thankful to Pakistan institute of nuclear science and Technology (PINSTECH) for giving me chance to work under great environment of laboratories which were best for research purposes.

A sincere thanks to all my friends Saba Noreen, Ayesha Bashir, Ambreen Akram, Sadia Tabassum, Faiza Munir and Munazza Jamshaid whose joyful company not only relaxed me in difficult moments but their support and help in daily life was also admirable. I also admire the behavior of Mr. Afzal and Mr.-Shakeel in NRG lab during my research work. I have no words to acknowledge the sacrifices, efforts, lots of prayers, support, guidance and firm dedication of my Mother and Father. My parent's prayers are always a source of my success. I also convey thanks to my sisters Samavia, Hanaf and Amna Zafar for their selfless love and endless support.

Anum Zafar

Abstract

Synthesis and characterization of Europium (Eu^{3+}) doped M-type barium hexaferrites ($Eu_xBa_{1-x}Fe_{12}O_{19}$; x=0.02, 0.04, 0.08, 0.1) is reported in this work. The electrical and magnetic properties of the synthesized material are investigated in detail as a function of doping concentrations. The material was synthesized using hydrothermal route from aqueous mixture of barium and ferric chlorides, and Europium nitrate. Reaction temperature was 180°C with 24 hours of reaction time. The synthesized powder was sintered at 900°C for 2 hours and pressed into pellets for subsequent impedance measurements.

The X-ray diffraction studies confirmed the hexagonal phase of the prepared samples with no secondary phase. The characterization of samples by SEM and TEM confirmed the spherical morphology for all the doped samples, however the sample with x=0.1 was a mixture of spherical and irregular shaped particles. Un-doped sample of the material exhibited a mixture of spherical and disc like structures with a diameter of 24.9±3.9. The particle size measured with SEM for x= 0.02, 0.04, 0.08 and 0.1 was, 50±33nm, 60.9±9nm, 70.5±8.9, respectively. The calculated sizes for x=0.02, 0.04, 0.08 and 0.1 were 23nm, 55nm, 65nm, 25nm and 102nm respectively through TEM. Fourier-transform infrared analysis was utilized to confirm the formation of hexagonal ferrites. FTIR graphs revealed the characteristics band of metal oxides and also specified the band region formed due to presence of water molecules.

A comprehensive study of the dielectric properties such as dielectric constant, dielectric loss tangents electric modulus and AC conductivity was performed in the frequency range 2Hz-2MHz. It is found that the dielectric constant, dielectric loss and tangent loss decrease with increase in frequency for a particular sample. However, these parameters increase with doping concentrations at a particular frequency. The dielectric properties have been clarified on the basis of hopping of charge carriers and Maxwell-Wagner model. The Ac conductivity and electric modulus increase as a function of frequency. The AC conductivity increases with doping concentration at low frequency while at high frequency the conductivity decreases. An equivalent circuit model was used to fit the Nyquist plot by Z-view software. The electrical behavior and relaxation process of the material was explained by Nyquist plot. Two semicircles were explained on basis of contribution from grains and grain boundary resistance.

The investigation of the magnetic properties was done by vibrating sample magnetometer (VSM) at room temperature. Saturation magnetization increases with doping concentration from 32.81 emu/g for x=0 to 54.39 emu/g for x=0.1. Similarly, the coercivity shows an increase with doping concentration from 0.4emu/g to 1.08emu/g. This makes our material very suitable for magnetic and high frequency recording media. The increase in H_c (0.4-1.08kOe) is caused by increase in magnetocrystalline anisotropy of material through doping.

Chapter 1

Introduction

Ferrites are mixed iron oxides$MO.Fe_2O_3$, where M can be any metal e.g. Sr, Ba, Pd, Co and have played an important role to mankind since earlier centuries. Such minerals were used as pigment in paints and in magnetic compass[1]. Recently ferrites have attracted wide attention around the World due to their enhance properties at nanoscale. In most of the magnetic media ferrites are used widely and have replaced other magnetic materials due to their superior properties. Ferrites are hard and brittle with high electrical resistivity then metals [2]. These are structure sensitive materials. Other than high resistivity ferrites have low eddy current losses, high permeability and moderate permittivity, high values of saturation magnetization and low dielectric losses. These extensive range of properties leads to application of ferrites in diverse fields [3, 4]. Ferrites are best suited materials for recording media, telephones, televisions, antenna rods, memory chips, activators, transducers and microwave applications [5]

The range of application expands more when these materials are reduced to nanoscale. For example, nanoparticles less then 20nm are supposed to be best suited for high density recording media and are currently under investigation. Ferrites are also used for magnetic resonance imaging (MRI), as catalysts, magnetic fluids and gas sensors [6]. Ferrites are highly sensitive to synthesis method, dopant, sintering conditions, amount of metal oxide present [7].

Ferrites are divided on the basis of structure as cubic vs. hexagonal and on the basis of magnetic properties as soft vs. hard. Soft magnetic materials are those which can be easily magnetized. These materials have narrow hysteresis loop and low saturation magnetization in addition to very small coercivity usually smaller then $1kAm^{-1}$ soft ferrites are used in stators, rotors and small transformers. Hard magnetic materials are not easy to magnetize or demagnetize and retain their magnetization often permanently. They have high coercivity which is usually greater than 10 kAm^{-1}. Hard ferrites are used as permanent magnets in loudspeakers, telephone receivers and automatic motors. Soft ferrites have very narrowed coercive filed as compared to hard ferrites[8].

The structure of M-type hexaferrites is composed of two basic formula units. The structure is built up from spinal blocks of two oxygen layers which are block S and S*. These blocks are connected by R block which can have barium, strontium or lead ions. This layer is considered to be hexagonally packed with respect to the oxygen layer on each side, also the four oxygen layers between them contains barium and are cubically packed. The plane (110) is basal plane and is the mirror of R block. The blocks preceding and succeeding the R block should be rotated over 1800 with respect to one another to maintain the symmetry. Five oxygen layers form one molecule and two molecules form one-unit cell of the structure. The structure can be written as RSR*S*[10]

The M-type ferrites have 64 ions per unit cell. These are distributed on 11 different symmetry sites. One-unit cell has 38 oxygen ions, 2Me ions and 24 irons ions. The Fe^{3+} ions are arranged on five sites 2a, 2b, 4f1, 4f2 and 12k. 2a 4f2 and 12k out of these five are octahedral 4f1 constitute tetrahedral symmetry and last 2b forms trigonal bipyramid as it is surrounded by five oxygen atoms. [11]. The oxygen ions are distributed 4e, 4f, 6h, and 12k sites and form a closed packed structure. The divalent or trivalent Me ions occupy the 2d sites. The arrangement of 12 Fe^{3+} ions is as follows:

- 12k sites have six iron ions with spin up
- 4f2 and 4f1 have 2 Fe^{3+} ions with spins down.
- 2a and 2b sites have one ion with spin up.

So eight Fe^{3+} ions have spin up and 4 have spin in downward direction which gives net magnetic moment of 4 per formula unit. Fe^{3+} ions have five unpaired electrons in the 3rd sell of d orbital according to electronic configuration. Each ion contains magnetic moment of 5μβ which gives the total moment 0f 20 μβ per formula unit [12]

1.2.1 Magnetic properties

On the basis of the magnetic properties materials are divided into different classes. Diamagnetism is normally shown by all materials. When these materials are placed in magnetic field, the atomic orbitals as a reaction adjust in such a way to produce a magnetic moment opposite to the applied field. Due to this effect the materials do not show any magnetic behavior in the magnetic field. This phenomenon is known as diamagnetism. The net magnetic moment per unit volume is termed as magnetization and is mathematically represented as

$$B=\mu H \qquad 1$$

Where B is magnetic induction (tesla) and H is the external field applied. In some materials, the atoms contain permanent magnetic moment which is caused by orbital and spin magnetic moments of materials [13]. In the absence of external fields, these moments are in random orientation which makes the net magnetic moment zero. But when an external magnetic field is applied, the magnetic moments already present in the material align themselves in the direction of applied field. This results in a non-zero magnetic moment. The alignment of the magnetic moments is distorted when external field is removed. The materials exhibiting spontaneous magnetization are called ferromagnetic materials. These materials maintain their alignment in magnetic moment even in the absence of external magnetic field. This implies that there is a strong intrinsic magnetic field within the material that keeps the magnetic moment aligned with each other [14]. The relationship between B and H in ferrimagnets is non-linear i.e. the materials show hysteresis when external field is applied.

1.2.2 Ferrimagnetic materials or ferrites

Ferrimagnetic materials are considered to be special class of materials. They exhibit almost all properties similar to ferromagnetic materials and also form hysteresis when exposed to external magnetic field. The difference between these two is in the way magnetic moments align due to exposure of external magnetic field. In ferrites all the spins and magnetic moment are not aligned in the same direction. The magnitude of these magnetic moment is also different then one another. Since these spin moments have different values, the net magnetization will be non-zero [15]. The origin of magnetic of coupling in ferrites is explained on the basis of super exchange interaction. In the crystal structure of hexaferrites, the cations are surrounded by the oxygen atoms; the chances of direct exchange between cations are therefore negligible. So super-exchange mechanism is expected to occur.

The super-exchange interaction in the hexaferrites is described as covalent bonding between the filled 2p-orbitals of oxygen and unfilled 3d orbital of cations. Exchange interactions are exhibited by the magnetic material when the electrons of the two different atoms interact which are present in the outermost shell. Further exchange interactions are divided into direct, super-exchange and double exchange interactions. [16]

1.2.3 Super-exchange interactions

Due to localized magnetic moments in oxides, the distance between these moments is very large and there is no possible approach for the direct interaction. In many oxides the oxygen atoms reside at the midpoint of the line which joins two magnetic cations. In such compounds, the magnetism phenomenon was explained by Anderson [17].

When oxygen atom shifts to its excited state, the 2p electrons shift to nearby metal cations temporarily. In case of ferrites we consider Fe^{3+}as neighboring cations which contains 5 electrons in d sub-shell arranged according to Hund's rule. The 2p electron from the oxygen atom jumps to Fe^{3+} and changes it to Fe^{2+} ion, which leaves an unpaired electron in the oxygen atom ready to interact with the Fe3+ on other side. This type of interaction between atoms is termed as super-exchange interaction. According to the structural configuration of ferrites as discussed earlier, the 4 up and 4 down spins are equal in magnitude cancelling each other and remaining five unpaired electrons of Fe^{3+} ions exhibit the total magnetic moment of 20 μβ[18]

1.2.4 Hysteresis loop

The ferrimagnetic materials, when exposed to external magnetic field follow hysteresis loop. This loop is also referred to as B-H loop. Figure 1.2 shows hysteresis curve for ferromagnetic

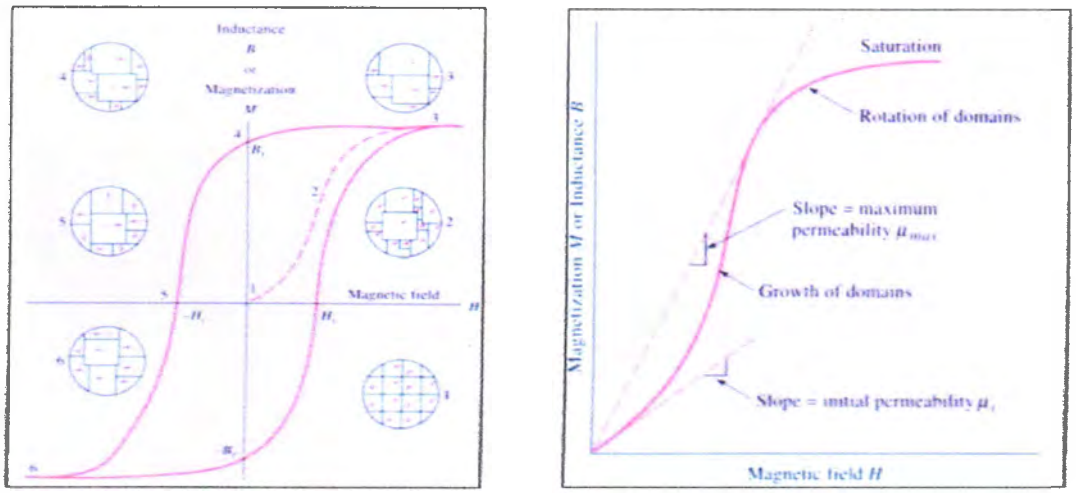

Figure 1.2: Hysteresis curve of ferrimagnets

materials. The magnetization of the material is increased when external filed is increased from zero. Initially when magnetization has a small value, the curve is linear.

When increased constantly, magnetization increases to its maximum and does not increase with further increase in the field. As the field starts to rise above the value of zero, the favorably arranged domains starts to grow in size and eventually all the spins present in crystal start to align in the direction of applied field [13]. This results in the formation of single large domain. At this stage the magnetization reaches its maximum value and further increase will not make any visible effect on the material. This point is called the saturation point or saturation magnetization Ms.

After reaching the saturation point, if the magnetization is gradually decreased to analyze the effect, the loop will follow a different path for demagnetization. This change of path for the magnetization demonstrates that, magnetization M_s lags behind the applied field B implying that at each value of B, the magnetization will have a higher value. When the value of B is reduced to zero, the magnetization will have a non-zero value. This value of magnetization is called remanent magnetization M_r. Fig 1.2 shows the demagnetization process from 3 to 5.

This parameter measures the magnetization of material in the absence of external magnetic field which determines the strength of materials as permanent magnet. As the field is increased in reverse order, the value of M_r starts to decrease. Figure 1.2specify this process from 5 to 6, the magnetization reaches to value of zero at B=-Bc. This field is termed as the coercive field. So the coercive field can be defined as the field required to completely demagnetize a permanent magnet. The further increment of magnetic field in the reverse direction gives the value of negative remanent magnetization M_r=-M_r. Now the curve forms a closed loop called hysteresis loop. Some energy is lost in this process during the domain alignment as the material is required to push domain back and forth. The impurities in the material can cause more hysteresis loss. The area under curve shows the energy loss [14].

1.3 Electrical properties

Solid materials are generally classified based on the ability to carry current at ambient temperature. Metals or conductors are good carriers of electricity at room temperature. The conductivity ranges from 10^4-10^6 S/cm. Insulators have the conductivity less than 10^{-10} S/m. the semiconductors have the conductivity range between 10^4-10^{-10}S/cm. Materials with high

conductivity at room temperature have the low energy of activation and vice versa. Most of the semiconductor and insulators show an increase in conductivity with an increment in temperature, whereas the conductors show slow and gradual decrease in conductivity with increase in temperature. The electrical properties in ferrites depend on number of factors including synthesis route and temperature, and doped materials. Ferrites have much higher resistivity then other metals. At room temperature the resistivity ranges from 10^{-2}-10^{11} ohm cm.

According to Verwey's model [18] the mechanism in ferrites responsible for conduction is hopping. The charge carriers hop between ions of the same element with variable valancies and random distribution over octahedral sites. The hopping depends directly between the conduction ions and the potential barrier. This potential barrier is known as the activation energy required for hopping [19]. The conduction of charge carriers in ferrites mainly occurs due to the hopping of electrons between Fe^{3+} and Fe^{2+} ions, when both the ions are located at the adjacent (octahedral) sides. This process also depends on the orbital intervention of oxygen ions with transition metal ions [20]. The hopping of electrons directly depends on the number of ferrous and ferric ions present in material [21]. M-type hexaferrites are hopping semiconductors with an efficient amount of mobile electrons [22].

1.4 Dielectric properties

Due to their higher electrical resistivity, ferrites have attracted the attention of scientists as the dielectric material. The study of dielectric properties shows how the electric field interacts with individual atom inside the materials. When we apply electric field to a dielectric material it gets polarized i.e. electric dipoles are created. The positively charged nucleus moves towards the direction of electric field while negatively charged electrons are pushed to the opposite direction. Now the nucleus and the electrons are at a relative distance 'r', the atom which was originally neutral acquires the electric dipole moment. Each dipole created during interaction with external electric field produced dipole moment which tends to interact with the external field. The induced dipole moment can be written as:

$$P=\alpha E \qquad 1.2$$

α Is known as the polarizability of atom.

The dielectric behavior of the material provides knowledge about the charge carriers, which helps to explain the conduction mechanism. The most important property of a dielectric material is its dielectric permittivity or dielectric constant which strongly depends on the frequency of time varying field. The dependence of dielectric field on the applied frequency is called dielectric dispersion. The reason for decrease in the dielectric constant is that the dielectric polarization fluctuations does not follow the frequency fluctuations.

When a dielectric material is exposed to external electric field, the polarization of material tends to change its direction with change in the polarity of applied field. When the frequency filed is low i.e. up to 10^6 then the polarity of material can follow the fluctuations without any significant lag and dielectric constant remains almost constant. If we increase the frequency up to 1MHz then the frequency fluctuations cannot be followed by the polarization of material it lags behind the frequency. Further increment of frequency in the range of 10^{10} Hz, causes the orientation polarization to cease as it cannot follow the fluctuations at all. This causes relaxation in dielectric material. Further increment of frequency will cause to cease all other polarization one by one. For example, in the infrared or far-infrared region (1013), ionic polarization is ceased, the response of electronic polarization losses its abilities in ultraviolet region around 1015 Hz. The low values of dielectric losses and dielectric constants enable the M-type hexaferrites to be effective for the application in microwave and surface mount devices [23].

1.5 Literature review

Singh et al. prepared the M-type barium hexaferrites via sol-gel synthesis. The observed the magnetic dielectric and structural behavior of the material at the ambient temperatures. The particle size synthesized during the studies was 49nm. The value of DC resistivity was measured to be 5.4x106 Ohm. With the coercivity value of 2151Oe, the saturation magnetization was 32.5emu/g[24].

Tang *et al.* observed the dielectric properties and scaling behaviors of strontium-cobalt-hexaferrites (Z -type hexaferrites) through impedance spectroscopy. The sample was prepared by solid state reaction method. The material was investigated under the temperature from 303-503K. The impedance spectroscopy shows that the electrical responses of the sample are thermally activated, with a distribution of relaxation times. The activation energies for grain and grain boundaries are calculated to be0.66 and 0.67eV. The results concluded that, although the

electrical response of the material was dependent on temperature, the relaxation mechanism was temperature independent[25].

Din *et al.* studied the influence of Cd substitution on various properties of M-type barium hexaferrites. The material was prepared by the co-precipitation technique and sintered at high temperature (1250°C). The crystallite size was found to be in rage of 26-27nm. The Dc electrical resistivity was observed to increase from 2.31x109 ohm cm to 6.42x109ohm cm. the value of coercivity was increased and a decrease in the saturation magnetization was observed from 33.5 to 9.2emu/g with an increase in the concentration of Cd[26].

Mallick*et al.* synthesized the M-type barium hexaferrites through co-precipitation and studied their dielectric properties. The synthesized particles were in the range of 80-100 nm. The sintering temperature was 1100-1300oC. The value of relative permittivity was 32 and low loss tangent 0.0329 was observed. This indicates that barium hexaferrites are suitable for high frequency applications[27].

Radwan*et al.* investigated properties of barium hexaferrites. The sample was synthesized through co-precipitation technique. It was observed during the studies that formation of single phase barium hexaferrites powders is achieved by decreasing the Fe^{3+}/Ba^{2+}molar ratio. The calcinations temperature was ≥1000oC. This resulted in good magnetic saturation (50.02emu/g) and wide intrinsic coercivity (642.4-4580Oe)[28].

Che*et al.* used the hydrothermal route to prepare the soft magnetic nanoparticles. The temperatures for the reaction were 140-180°C. The saturation magnetization was 1.1emu/g with the coercivity 221 Oe. The treatment of sample to an annealing temperature of 800°C led to an order-of-magnitude increase in the value of saturation magnetization and coercive force which were 4511 Oe and 67.3emu/g respectively. As a result it was suggested that the oxygen vacancies should be responsible for the magnetic behavior that appeared for barium hexaferrites[29].

Khan et al. observed the effect of Pr-Ni substitution in $Ca_{0.5}Ba_{0.5-x}Pr_xNi_yFe_{12-y}O_{19}$prepared by sol-gel auto combustion technique. The XRD analysis confirmed the preparation of single phase nanoparticles. The Pr-Ni was observed to be completely soluble in the lattice. Transmission electron microscopy revealed decrease in the grain size with increase in Pr-Ni substitution. The coercivity values of prepared samples were all in the range of M-type hexaferrites[30].

Almeida *et al.* analyzed the M-type barium hexaferrites through impedance spectroscopy. The sample was prepared by the ceramic method. The main idea of the study was to observe the electric properties as a function of synthesis parameters i.e. milling time and milling power. The study revealed that milling parameters strongly affect the electric properties such as dielectric constant, which increases with an increase in the milling power. Impedance and dielectric loss were also observed to change with milling power[22].

Zi *et al.* prepared the Co-Ce substituted M-type barium hexaferrites by simple co-precipitation method. X-ray indicated single phase formation of nanoparticles. Increment in the coercivity field Hc was observed at low substitution and reaches at maximum with x=0.1. The results showed that the prepared material can be a promising candidate for permanent magnets and perpendicular recording media[31]

X Battle *et al.* investigated the distribution of cations and magnetic properties with the doping of Co-Ti in M-type barium hexaferrites ($BaFe_{12-2x}$,Co_x,Ti_xO_{19}). The techniques used for investigation was neutron powder diffraction method and high field magnetization. The Co ions (50%) occupy octahedral sites according to studies which makes it ineffective in magnetic isotropy. While Ti ions lie in the 4fVI sites producing a strong local spin and contributing in the magnetic properties of material [32].

Jacobo *et al.* synthesized the ultrafine M-type barium hexaferrites through chemical co-precipitation. The precursors were precipitated by adding barium salt to strongly alkaline ferrate solution. Solution was heated to 800oC for 6h to yield the desired product. The scanning electron microscopy of the powders revealed that the particles were less then 5µm in diameter[33].

Nasir *et al.* enhanced the electric and magnetic properties of Ni–Zn ferrites ($Ni_{0.5}Zn_{0.5}Cr_xMn_{0.5x}Fe_{1-x}.5O_4$) synthesized by sol-gel method. The products shoed high saturation magnetization, low dielectric loss and low coercivity values. From 1 MHz to 1.3 GHz the dielectric loss almost remains the same as Cr amount was increased. Crystallite size and lattice parameters also remained constant. The coercivity values were observed to decrease while the saturation magnetization was unaffected up to x=0.4[34].

Mallick *et al.* substituted cobalt in M-type barium hexaferrites for the observation of magnetic properties. The sample was prepared by the co-precipitation method with 1, 2, 3, 5, 10, 15, 20 and 30 wt% cobalt oxides. Permeability and magnetic loss tangent was increased to a value of

3.5 at 5% doping. The saturation magnetization was reduced from 87emu/g to 58emu/g where remnant magnetization was increased with an increase in doping concentration. A sharp increase in Hc was observed from 540 to 2200 Oe. The compounds revealed variation in densities 4.45 g/cm3. The structure was also changed to W-type hexaferrites during substitution[35].

Pereira *et al.* discussed magnetic and dielectric properties of M-type barium hexaferrites with a substitution of strontium ($BaxSr_{1-x}Fe_{12}O_{19}$), in RF and microwave (MW) frequency range. The sample was synthesized by new ceramic method. The sample revealed lower tangent loss (Tanδ = 4.10-3 at 1.5 GHz). The coercivity of the sample was observed in the range of 3–5 kOe and remanence magnetization in the range of 33–36 emu/g [36].

Dimri *et al.* used citrate precursor method to synthesize the barium hexaferrites nanoparticles. They concluded that the particle size can be controlled by controlling the pH of the solution. The sample prepared from solution with pH 5.25 shows 2-3 folds higher dielectric loss and dielectric constant as compared to other two samples having pH 1.88 and 9.0 as the precursor solution[37]

Abbas *et al.* analyzed Electromagnetic and microwave absorption properties of barium hexaferrites and its polymer composite. The composites were also substituted with Co^{2+}–Si^{4+}. The synthesis method used was solid state technique. At higher gigahertz frequencies the permeabilities of the sample were reduced. Throughout the measured frequency range the μ' and μ'' remained almost 1 and zero. Both sintered ferrite and composite absorbers can be used for suppression of electromagnetic interference as well as in stealth technology[38].

Lisjak *et al.* used ethanol precipitation for synthesis of Barium hexaferrites nanoparticles with various precipitation and calcination conditions. The replacement of ethanol with water provided the chance to decrease the formation temperature well below 1000°C, the homogeneity of the structure was also reported to be improved. It proves simple method for low temperature synthesis of barium hexaferrites[39].

F. Khademi *et al.* doped barium hexaferrites with europium ($Ba_{1-x}Eu_xFe_{12}O_{19}$) and discussed their structural, magnetic and microwave properties. The results showed decrease in size of particles as material was doped with Eu. An increase in coercivity with decreased saturation magnetization was observed. The material revealed the reflection loss of -43 dB at frequency range of 12-18 GHz, suggesting the material to be applicable in microwave devices[40].

Costa *et al.* discussed the dielectric properties of the lead doped(PbO)-Co_2Y type hexaferrites ($Ba_2Co_2Fe_{12}O_{22}(Co_2Y)$) prepared by solid state reaction method. The frequency range for dielectric and electric modulus properties was 1Hz-1MHz. the temperature range was selected between 313-493K with complex impedance spectroscopy technique. The material shows non-exponential type of conductivity relaxation. The impedance plot was comprised of two semicircles which pointed out grain effect and grain boundaries. The activation energy revealed similar behavior in material with all doping concentrations[41].

Hayat *et al.* analyzed the electro-active regions of $BaMnO_3$ with impedance spectroscopy. The material was prepared by conventional mixed oxide route. The material shows semiconducting behavior with electrical inhomogeneity. The electro-active regions overlap in applied frequency domain. The Nyquist plot suggested the grain and grain boundary regions. The conduction mechanism was explained by CBH model[42].

Singh *et al.* studied the effect of rare earth ions substation effect on strontium hexaferrites with different molar substitutions. The ions of lanthanum, neodymium and samarium were doped by standard ceramic technique. The electrical properties of the material were analyzed in frequency range of20Hz to 1MHz. the trends in electrical properties were explained by Koop's model and Maxwell-Wagner model. increase in magnetic properties e.g. magnetizing moment, coercivity and Curie temperature was observed with doping concentrations[43].

1.6 Motivations and objectives

M-type hexaferrites are most widely used materials for electronic application such as permanent magnets, magnetic recording and microwave devices. Their unique properties at high frequency make them suitable for RF and microwave applications. Due to these extraordinary behavior and properties these materials are under investigation from decades. Ferrites are highly resistive material which makes them suitable for application in electronic devices. The high resistivity of these materials restrains the eddy current losses. The ferrites material useful in magnetic industry are required to have large saturation and remanence magnetization

To gain the above mentioned objectives, the partial replacement of Ba with rare earth ions is attempted. Since rare earth ions are insulators with high electrical resistivity, they are expected to

enhance the electrical resistivity at high frequency and low eddy current losses. To improve the magnetic properties of $BaFe_{12}O_{19}$, the substitution of Fe^{3+} and Sr/Bm^{3+} with some of the rare earth ions has been reported earlier[43]. The electronic shell structure of the rare earth ions is unique and makes it suitable for variation in magnetic properties through different doping concentration in the material. The effect of different doping concentrations of Eu^{3+} will be studied on different properties of M-type barium hexaferrites. The effect on dielectric constant, dielectric loss, conductivity tangent loss and magnetic properties will be observed with variation in doping concentration.

Chapter 2

Characterization Techniques

2.1 X-ray diffraction

To analyze the structural properties of the material, X-ray diffraction technique was used. This technique provides us the structure and phase identification of the materials. This technique is based on the fact that X-ray is in comparable range to distance between atoms in crystals. The crystal act as well defined and extended grating material to diffract the X-rays and shows a pattern with many sharp points. The interaction of X-rays with the crystalline material is based on Bragg's law [44].

According to Bragg's law the X-ray reflects from the series of the plane of the crystals. When the angle of incident equals the angle of reflection maximum reinforcement of the waves occurs. Waves from the successive layers reinforce when their path difference is the integral multiple of 'λ'. Consider a crystallographic structure with the distance 'd' between the planes with the wavelength 'λ' of the incident X-rays, then according to Bragg's law:

$$\lambda = 2d\sin\theta \qquad 2.1$$

Where 'θ' is the angle between the crystal plane and incident beam. When the waves interfere constructively, the equation becomes:

$$n\lambda = 2d_{hkl}\sin\theta \qquad 2.2$$

Where 'hkl' is the miller indices of the structure. The constructive interference shows sharp peaks which determine the phase of the crystal [45]. The crystallite size of the sample is calculated by Scherrer formula, by using the Full-width at half maximum of the observed peaks.

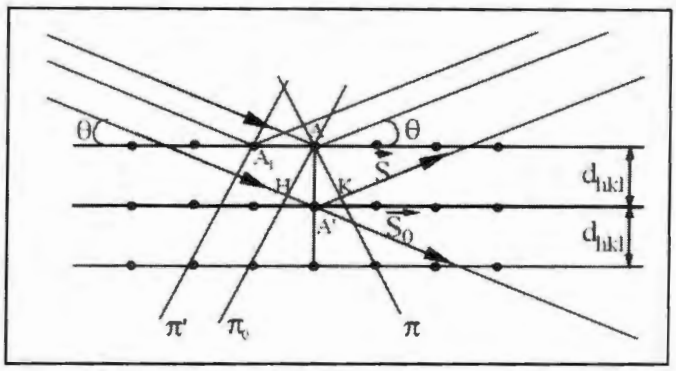

Figure 2.1: Geometrical representation of Bragg's law [16]

Mathematically:

$$D = \frac{0.89\lambda}{\beta\cos\theta} \qquad 2.3$$

Where' λ' is the wavelength of X-rays 'β' is full width at half maximum and 'θ' is the Bragg's angle. Figure 2.1 demonstrates the law geometrically.

2.2 Scanning electron microscopy (SEM)

Scanning electron microscope is used to observe the morphology of the prepared structures. The electron sources used in SEM are tungsten filament, Shottkey emitter or field emission [46].The electron gun produces a high energy beam of electrons which strikes the surface of the sample. The beam passes through magnetic lens and deflecting plates which deflects the electron beam into horizontal and vertical axis, so that whole surface of the image can be imaged properly. When the electron beam strikes the surface of sample, surface releases energy in form of X-ray photons and electron which are detected by the detector. The detector converts the released energy into signals. These signals make a final image of the sample on the screen. The figure 2.2 shows the scanning electron microscope used in characterization of samples in this work.

Figure 2.2: SEM setup at Institute of Space Technology (IST), Islamabad

2.3 Energy dispersive X-ray spectroscopy

The EDS is used to analyze the structure and component of the elements in the material. It uses the emitted X-ray spectrum from the solid material to obtain a localized chemical analysis. It can detect all the chemical elements from Be-U. The primary analysis involves the production of X-ray spectrum from the entire scan area of SEM. The qualitative analysis of the specimen is done on the basis of identification of X-ray spectral lines which is fairly straightforward. The quantitative analysis in EDS i.e. presence of each chemical in the sample require measuring the intensity of lines obtained for each element[47].

2.4 Transmission electron microscopy

The transmission electron microscope (TEM) is a technique to analyze the morphology of the sample using electron beam. The electron gun produces the beam using the voltage which ranges from 50-150 kV. The power of electron beam depends on the voltage provided. It means that the higher the voltage is, shorter is the electron beam wavelength and more precise and magnified the image is. The Figure 2.3 shows the working principle of TEM.

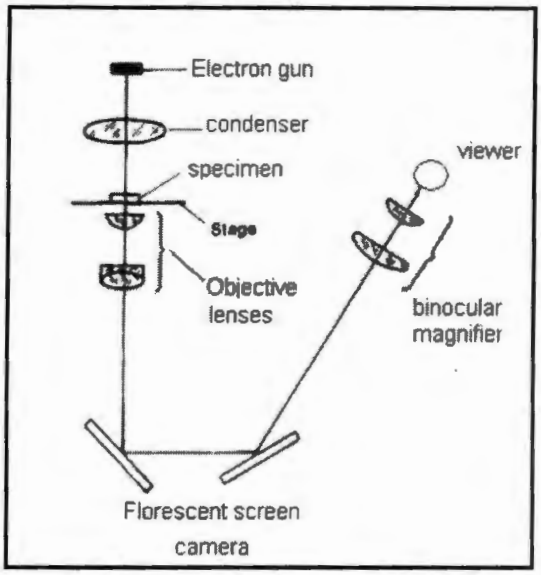

Figure 2.3: Schematic representation of TEM [48]

The beam of electrons is accelerated to high energy levels through voltage applied. This electron beam can scatter or backscatter elastically on inelastically. In addition to scattering, these beams can produce X-rays Auger electrons or light. The image is formed when the beam is transmitted through the specimen. The image is magnified and focused on screen or a detector as CCD camera[48].

2.5 Fourier-Transform Infrared Spectrometers (FT-IR)

To examine the molecular fingerprints of the sample Fourier transformed infrared spectrometer was used. In FTIR, absorption and transmission of IR rays is used to analyze the sample providing information about the molecular bonding present in the specimen. The FTIR can identify unknown material; determine the quality and consistency of sample. It is useful to determine the amount of components in a mixture [49]. FTIR operates on a principle called Fourier transform.

Mathematically:

$$F(w) = \int_{-}^{+} f(x)e^{i\omega x}\,dx$$

The inverse of Fourier transform is expressed as:

$$f(x) = \frac{1}{2}\pi \int_{-}^{+} F(\omega) e^{-i\omega x}\, d\omega$$

Where 'ω'represents the angular frequency, x is the optical path difference, and F (ω) is the spectrum with f(x) being interferogram. f(x) is determined experimentally and F(ω) can be determine by applying Fourier transform[50].

2.6 Impedance spectroscopy

Impedance spectroscopy is one of the most important techniques to analyze the electrical properties of any material. Generally, a material is DC biased to measure the electrical properties but it results in polarization of charges at the interface of electrode and electrolyte. This polarization opposes the applied field which causes the ionic current to fall with time. Four probe method is used to avoid this problem [51].Generally the impedance is defined as the collective opposition offered by a circuit to a flow of alternating current. Impedance is a complex vector and can be represented on a graphical plane. It consists of a real part (resistance) R and an imaginary part (reactance). Figure 2.4 shows complex plane representation of impedance. It is represented as rectangular coordinate form as R+jX.

And in the polar form as:

$$|Z| < \theta \qquad 2.6$$

$$R + jX = |Z| < \theta \qquad 2.7$$

$$R = |Z| \cos\theta \qquad 2.8$$

$$X = |Z| \sin\theta \qquad 2.9$$

$$\theta = \tan^{-1}\frac{R}{X} \qquad 2.10$$

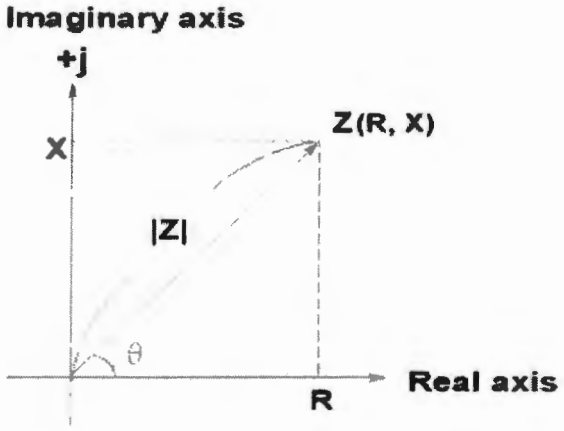

Figure 2.4: complex plane representation of impedance [52]

Z^* is called the complex impedance. And can be represented as:

$$Z^* = Z' + iZ'' \qquad 2.11$$

Where Z' is the real part of impedance and Z'' represents the imaginary part[52].

2.6.1 Impedance of RC circuit

The electrical response of materials is calculated in terms of electrical impedance as a function of frequency. Different types of impedance plots represent the electrical response of the material under investigation. Various conduction mechanisms can be studied with the help of impedance plots. The Nyquist plot between Z' and Z'' provides best way to investigate different electro active regions in the material and their conduction mechanism as well. An equivalent circuit model is used for better approximation with the experimental data, which contains resistor, capacitor and other elements as well[53]. We imagine an RC series circuit with a capacitor and a resistor. The sum of all individual components impedance corresponds to the resultant impedance in the present condition. The resultant impedance can be represented by the following equation.

$$Z_s^* = R_s - j\frac{1}{\omega C_s} \qquad 2.12$$

This equation represents a straight line complex plane. The line has negative slope and intercept on real axis at $R_s$as shown in figure. Usually a semicircular arc in a complex plane is the outcome of experimental data in case of a parallel circuit. The semicircle has the centre at the real axis and can be fitted by using the circuit having a resistor and a capacitor in parallel. The radius of

semicircle represents the resistance of the material under investigation. Smaller the radius of the semicircle, smaller will be the resistance of the sample and vice versa. Figure 2.5 shows parallel and series circuits with their complex plane representations.

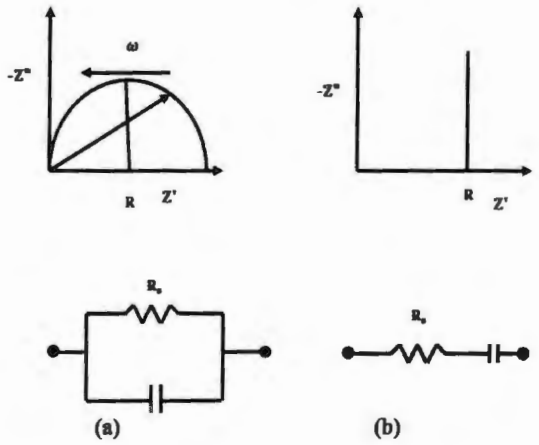

Figure 2.5: (a) complex impedance of parallel circuit (b) complex impedance of series circuit

2.6.2 The constant phase element

Most of the materials generally do not follow the ideal capacitive behavior. The deviation can be caused by inhomogenity in the sample which depends on the crystallinity, porosity, surface roughness and defects in the crystal lattice. This deviation is called constant phase element. The defects in the material mentioned above cause distribution of relaxation times instead of a unique relaxation point. This phenomenon was first explained by Fricke [54].

For parallel combination of R (resistor) and C (capacitor or Constant phase element), impedance measurements result in semicircular arc in complex plane shown in figure 2.6. The dashed line shows behavior of constant phase element in parallel circuit while the solid line represents capacitive behavior

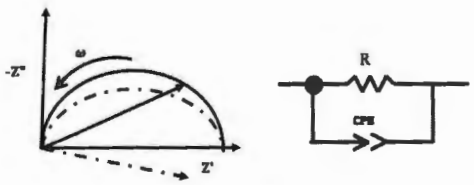

Figure 2.6: (a) CPE behavior (dashed line) and ideal capacitive behavior of RC parallel circuit (b) parallel circuit with CPE

2.6.3 Dielectric permittivity

The mechanism of polarization in ferrites is similar to the conduction i.e. by electron exchange between Fe^{2+} and Fe^{3+} ions. The electrons displace locally in the direction of applied filed which determines the polarization in material.

The complex dielectric permittivity can be expressed by the equation:

$$\varepsilon^* = \varepsilon' + j\varepsilon'' \qquad 2.12$$

Where ε' represents the dielectric constant or permittivity and ε'' is the dielectric loss and 'j' is the complex number. In the present study the values of ε' and ε'' were calculated by the pellet dimensions, measured impedance data and following equations.

$$\varepsilon' = \frac{t}{\omega A \varepsilon_0}\left[\frac{Z''}{Z'^2+Z''^2}\right] \qquad 2.13$$

$$\varepsilon'' = \frac{t}{\omega A \varepsilon_0}\left[\frac{Z'}{Z'^2+Z''^2}\right] \qquad 2.14$$

'ω'represents the angular frequency 'A' is the area of pellet 't' is the thickness of pellet and 'ε_0' is the dielectric constant (8.85×10^{-12})

2.6.4 Dielectric loss tangent

The ratio of dielectric constant ε' and dielectric loss ε'' is called the dielectric loss tangent.

Dielectric loss tangent describes the energy loss in the material. Dielectric loss is caused when the polarization lag behind the alternating frequency. The cause of polarization lag can be the imperfections and impurities in the sample.

$$\text{Tan}\,\delta = \frac{\varepsilon''}{\varepsilon'} \qquad 2.15$$

2.6.5 Electric modulus

Reciprocal of dielectric permittivity is called electric modulus and is denoted by M. Complex electric modulus is expressed as

$$M^* = \frac{1}{\varepsilon^*} \qquad 2.16$$

$$M^* = M' + M'' \qquad 2.17$$

The complex electric modulus shows the measured ion energy distributions in the material and also explains the electrical relaxation points of materials [55]. The electric modulus explains the dynamic properties of the sample only as it suppresses the effects occurred due to polarization at electrode-electrolyte interface. In the present study the corresponding values of M' and M" were calculated by using the formulas as follows.

$$M' = \frac{\omega A \varepsilon_0 Z''}{t} \qquad 2.18$$

$$M'' = \frac{\omega A \varepsilon_0 Z'}{t} \qquad 2.19$$

Where $\omega$is the angular frequency, A is the area of the pellet and t is the thickness of the pellet [56].

2.6.6 AC conductivity

In the present study the conductivity of each sample was calculated by using the following equations.

$$\sigma_{Ac} = \omega\, \varepsilon_0 \varepsilon'' \qquad 2.20$$

Or

$$\sigma_{Ac} = 2\pi f \varepsilon_0 \varepsilon' tan\delta \qquad 2.21$$

2.7 Vibrating sample magnetometer (VSM)

The characteristics of any magnetic material are best observed and described in form of hysteresis loop. To analyze the magnetic behavior of the ferrites, vibrating sample magnetometer is used at room temperatures in present study. VSM can measure the magnetic properties of the material with magnetic field, temperature and time.

Vibrating sample magnetometer is based on Faraday's law which states that when there is a change of flux in the coil, electromagnetic force is generated around it [14]. Fig 2.7shows the schematics of a VSM. In the VSM setup, the sample moves between the proximity of two pickup coils. The transducer assembly translates the sinusoidal signal provided by the oscillator in vertical vibrations. The sample is fixed with the sample stage which vibrates with provided frequency and amplitude. The sample is placed at the center of two poles made from electromagnets generating magnetic field H_0. Pickup coils are stationary and placed on the poles of electromagnets having the same magnetic centers [57].

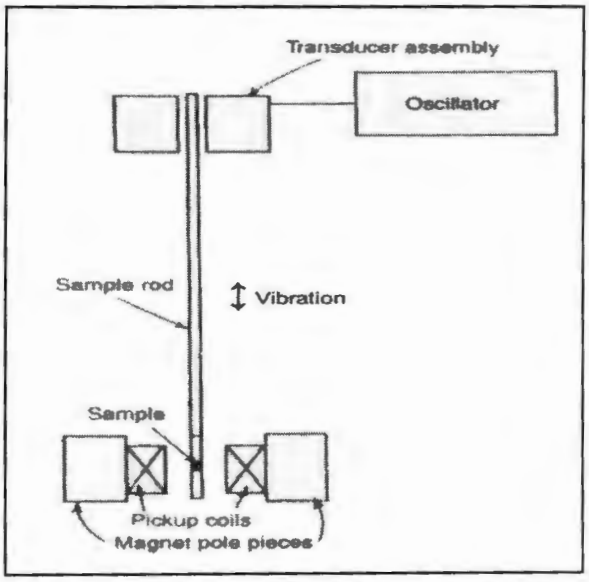

Figure 2.7: Schematic representation of VSM

Chapter 3

Experimental Procedure

3.1 Synthesis techniques

The properties of any material are greatly dependent on their micro or macro structures. Nanoparticles are highly structure sensitive materials. Most of the properties of these materials depend on structural stability, porosity, vacancies, grain size and phase purity which can be controlled by synthesis conditions and synthesis routes followed. Scientists have followed and developed different synthesis techniques. Two most frequently used routes for synthesis of nanomaterials are solid state reaction methods and wet chemical methods.

3.2 Solid state reaction method

The solid state reaction method combines individual oxides in stoichiometric ratios and are grounded well to achieve homogenous mixture. Normally this technique is termed as top down techniques as the material is grinded into powder form to obtain the nanoparticles. The grinding can be achieved by different methods motors pestle and ball milling. The powder is then annealed for a longer time at elevated temperatures. The particle size achieved through these techniques is quite large with wide size ranges. The phase impurity is a challenge in solid state reaction methods. [58-60].

3.3 Wet chemical methods

Wet chemical methods commonly known as bottom up methods, are non-conventional techniques and have better phase purity then top down techniques. These techniques include:

- Microemulsion method
- Spray-drying methods
- Hydrothermal methods
- Co-precipitation method
- Sol-gel method
- Freeze-drying method

3.3.1 Microemulsion method

The dispersion of two immiscible liquids stabilized with the help of active surface agent is called Microemulsion [59]. The solution is a mixture of surfactant oil and water whereas the oil is the mixture of hydrocarbons and olefins. An interface is formed during the synthesis which is between water and oil. The surfactant is most important precursor for the production of M-type hexaferrites, different surfactants have been usedin studies [59-61] . Microemulsion is a high cost technique and yields very small amount of materials as well as face reproducibility problems.

3.3.2 Spray drying method

In the spray drying method the solvent is evaporated from concentrated solution of cations to form the precipitates in material. To retain the small size of the particles the cationic solution is transformed into small droplets with the help of elevated pressure. To remove the solvent, hot stream of gas is used. Small sized particles are obtained through this procedure which are then converted into compact powder and anealed to suitable temperatures.

3.3.3 Freeze drying method

The conversion of concentrated solution of cations through freeze droplets, by passing them a bath through very low temperature is called freeze drying method. For this purpose, liquid nitrogen or ice-acetone is used. The obtained particles are dried through sublimation in vacuum.

3.3.4 Precursor method

Precursor method allows us a precise stoichiometry for the synthesis of materials. The required amount of reactants is used as precursors. These precursors are then decomposed through heating to form the required material.

3.3.5 Sol-gel method

Commonly known as chemical solution deposition method, this method is extensively used for production of nonmaterial. The precursors used generally are metal chlorides and alkoxide the mixture of precursors (sol) is then converted into solid termed as gel. The drying process removes some of the solvent remaining in the gel. After heat treatment the gel is converted into required material. The density and crystallinity of the material is improved by this material.

Many factors like temperature pH and solution composition greatly affect the particle size[58]. The required time and temperature for drying is quite high in this procedure.

3.3.6 Co-precipitation method

The co-precipitation method is most widely used method for the production of nanomaterials. In this method, a solution of salts is prepared which are required for final compound. Mostly water soluble salts are used in the technique, but the insoluble salts are used with acids to mix them water. All the salt solutions are mixed and a precipitating agent is added which is basic. Mostly NaOH and KOH are used. With the addition of precipitating agent, precipitates are developed with agglomeration and gr owth of gra ins. The agglomeration a nd grain growth depends on the pH, stirring sped and solution temperature as well. During the reaction chlorides, acetates and nitrates are removed by washing process. Heat treatment helps to overcome hydroxides formed during synthesis reaction.

3.3.7 Hydrothermal method

Hydrothermal method uses high temperature and pressure to crystallize the required material. Hydrothermal process takes place in a closed container called autoclave to maintain high temperature and pressure. Water is used as a solvent in this technique. The aqueous solution is heated in autoclaves at high temperature, which produces and maintains a high pressure inside the container. The reaction which takes place at such high pressure is called hydrothermal reaction. As the temperature of the liquid is increased and is above its critical point, it behaves as both liquid and gas and is said to be supercritical. At the supercritical stage the surface tension of the liquid is almost negligible and compounds are dissolved easily. The critical temperature for water is 374°C. After the reaction the solution is washed several times to remove the water soluble impurities. The solution is also washed with ethylene to improve its purity. The solution is then dried at suitable temperature and powder is obtained which is then grinded for fine powder. Strontium hexaferrites have been synthesized with this technique. In the present study, hydrothermal technique is used due to its greater reactivity high purity and fine particle size distribution. Hydrothermal is also a low cost method which makes it more suitable for synthesis.

3.4 Experimental procedure

The Europium doped M-type barium hexaferrites ($Eu_xBa_{1-x}Fe_{12}O_{19}$) were prepared by hydrothermal technique in the present study. All the chemicals used in the procedure were of analytical grade. The required molarities of the metallic salts of Iron, Barium and Europium were mixed in deionized water. The salts used in the procedure were iron chloride ($FeCl_3$) and barium chloride di-hydrate ($BaCl_2.2H_2O$). Sodium hydroxide was added drop wise to form the precipitates at pH 14. The mixture was stirred for 15 minutes for fine mixing.

The prepared solution was heated in oven at 180°C in the autoclaves to build a high pressure in container and to start the reaction as well. The reaction time for the experiment was 24 hours. After the reaction the solution was washed with de-ionized water 3 times. The solution was also purified by sonification bath to remove impurities from lattice through vibrations. The particles were separated from the solution through centrifuge. The solution was centrifuge 3 times with water and once with ethanol for more purification. The separated particles were dried at 70°C for 24 hours. Fine powder of particles was obtained after drying which was grinded with Agate mortar-pestle. The prepared powder was annealed at 900°C for 2 hours. The chemicals used in the experiment are listed in table 3.1.

Table 3.1: Chemicals used in experiment with specifications

S. No.	Compound	Formula	Purity	Molar Mass	Manufacturer
01	Barium Chloride di-hydrate	$BaCl_2.2H_2O$	99%	244.27g/Mol	Reidel-de Haen
02	Iron(III) Chloride	$FeCl_3$	99%	162.21g/Mol	Merck
03	Sodium Hydroxide	NaOH	98%	40.0g/Mol	Merck
04	Europium nitrate(III) pentahydrate	$Eu(NO_3)_3.5H_2O$	99.9%	428.06g/Mol	Merck

3.4.1 Sample preparation for impedance spectroscopy

For impedance spectroscopy the powder was pressed into pellets with a force of 383kN/m^2. No binding material was used in the sample during the preparation of pellets. Prepared pellets were annealed at low temperature (100°C) for compaction and removal of water absorbed. The pellets were 10.1mm in diameter. The thickness of pellets with composition x=0.04, 0.08 and 0.1 were 1.4mm in diameter while 0.02 had the thickness of 1.6mm. The pellet of un-doped sample was 3.8mm in thickness. Figure 3.1(a &b) shows prepared pellets in this study.

Silver paste was used to make contacts on both sides of pellets. Contacts were then heated to 150 °C for 1 hour. LCR meter was connected through these contacts with copper wires. Agilent E4980A LCR meter was used for impedance measurement with frequency range from 2Hz to 2MHz.

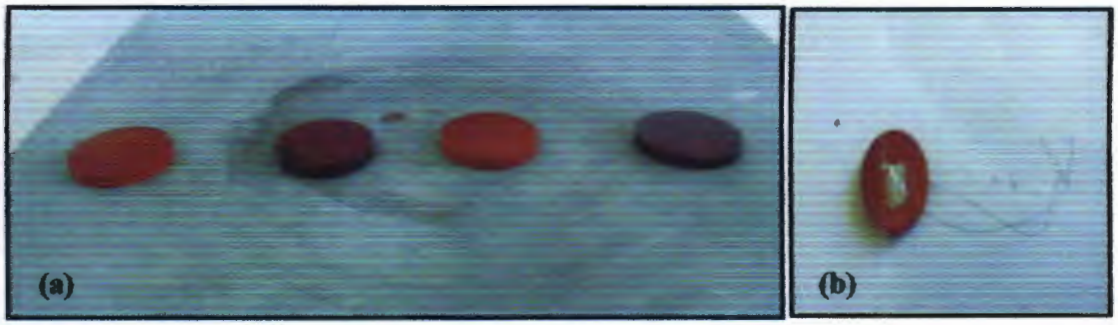

Figure 3.1: (a) Pellets of the prepared samples (b) prepared pellet with contacts

Chapter 4

Results and Discussion

4.1 X-ray diffraction

The X-ray diffraction pattern for un-doped sample indexed with (hkl) values for each peak of barium hexaferrite is demonstrated in figure 4.1. The observed pattern indicate no extra lines and is in well correspondence with the standard pattern of $BaFe_{12}O_{19}$in accordance with JCPDS file no. 27-1029. This indicates that the prepared sample has a single phase hexagonal structure and no impuritiy is present in sample. The iron in the material leads to high level noise in the XRD spectrum background because it flouresces as the radiation energy of CuKα radiation is quite close to Fe energy states [27]. The difference in the inetsity of the peaks from the refference JCPDS file is due to preffered orientation of hexagonal plates in the structure [35].

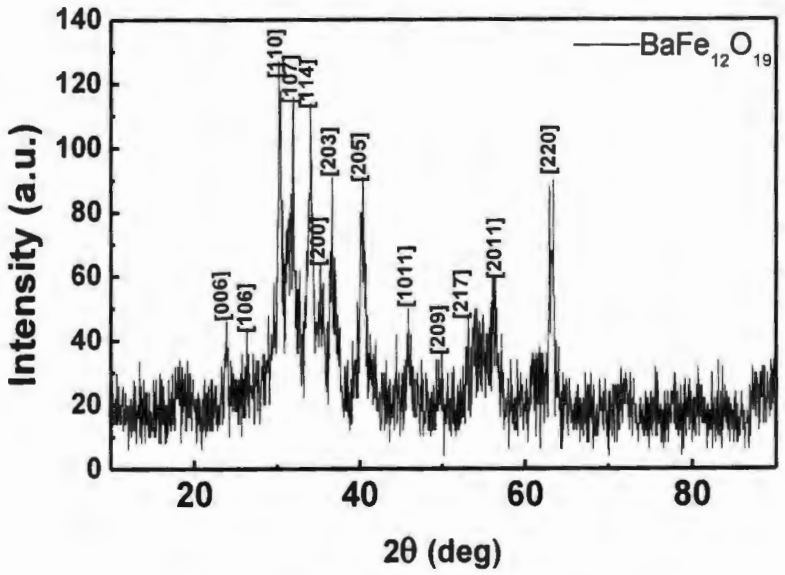

Figure 4.1: XRD pattern of $BaFe_{12}O_{19}$

The structural analysis of doped samples with concentrations x=0.02, 0.04, 0.08 and 0.01 is revealed in figure 4.2. The graph shows that the samples are generaly single phase corresponding with JCPDS card no.043-0002. No extra phase was detected other than hexagonal phase of the material which suggests that Eu arranges in hexagonal structure. The peaks position slightly

changes which can be attributed to stress and strains in the crystal structure. Crytallinity of the synthesized structure was improved with doping in present study.

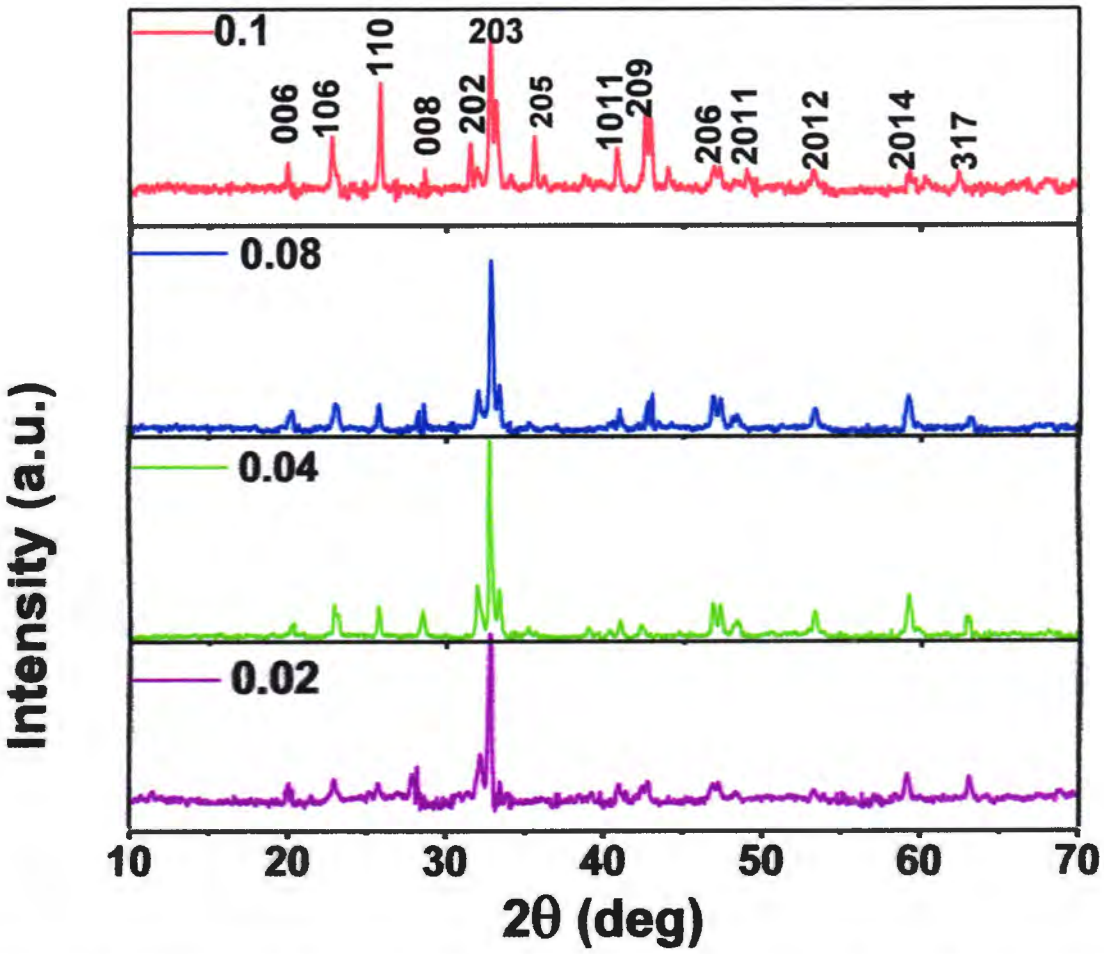

Figure 4.2: XRD pattern for $Eu_xBa_{1-x}Fe_{12}O_{19}$ nanostructures, with x = 0.02, 0.04, 0.04 and 0.1.

4.2 Scanning electron microscopy

The surface morphology of the prepared material is analyzed through field emmission scanning microscope. The micrographs of un-doped barium hexaferrites are shown in figure 4.3 and reveal the formation of mixed particles and circular discs. The average size of the discwas found to be 24.9 ± 3.9 nm.

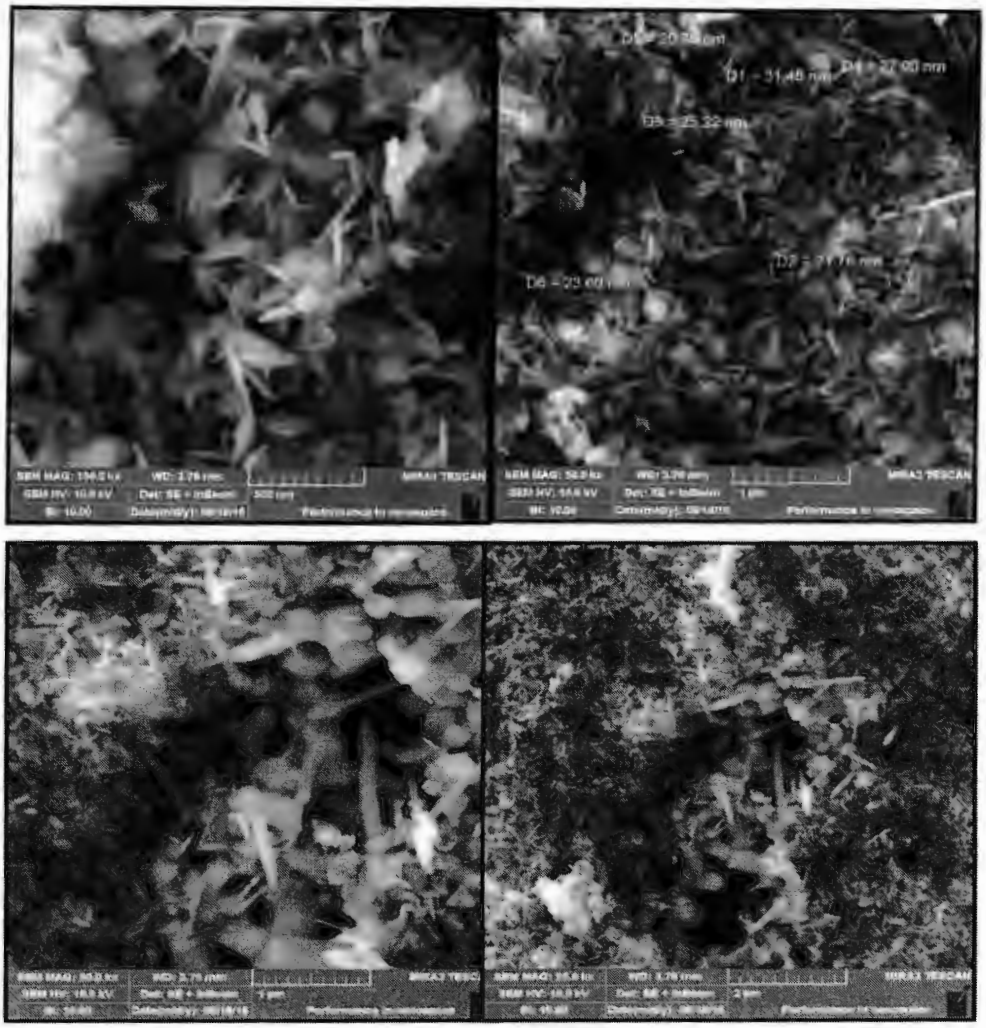

Figure4.3: SEM micrographs for $BaFe_{12}O_{19}$

The micrographs of sample doped with Eu x= 0.02 are shown in figure 4.4. The images reveal formation of agglomerated nanoparticles in sample. The agglomeration of particles can be attributed to magnetic nature of the nanoparticles. The average particle size was calculated to be 50.1±1.33 nm. The particle size thus increases compared to the un-doped sample.

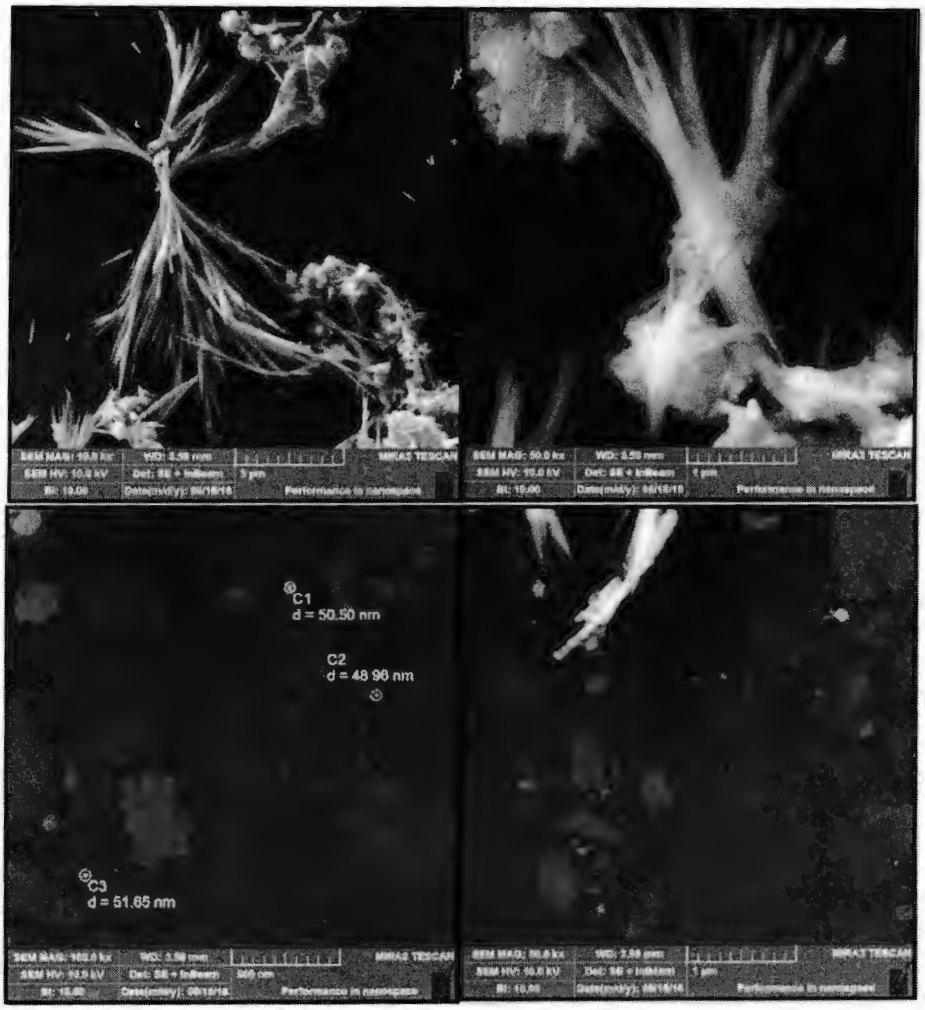

Figure 4.4: SEM images for sample doped with x=0.02(Eu)

The morphology of barium hexaferrites doped with x= 0.04 and 0.08 are shown in figure 4.5 and 4.6 respectively. The average particle size in the sample with x= 0.04 is 60.9±6.8 nm and in sample with x= 0.08is 69±16 nm. The error in the average size of all the samples is the standard deviation calculated by taking average of at least 15 particles. The particle size in the material is increasing as in all the other samples.

The morphology of the sample with $x = 0.1$ (Eu) is shown in figure 4.7 revealing again the formation of spherical and irregular shaped nanoparticles in the sample. The average particle size is 70.5±18.9 nm. The particle size evidently increases in each sample with doping.

The SEM reveals the formation of nanoparticles with different sizes range from 24-70 nm with no considerable change in particle shape except with sample x=0, the particle shape changes from discs to particles.

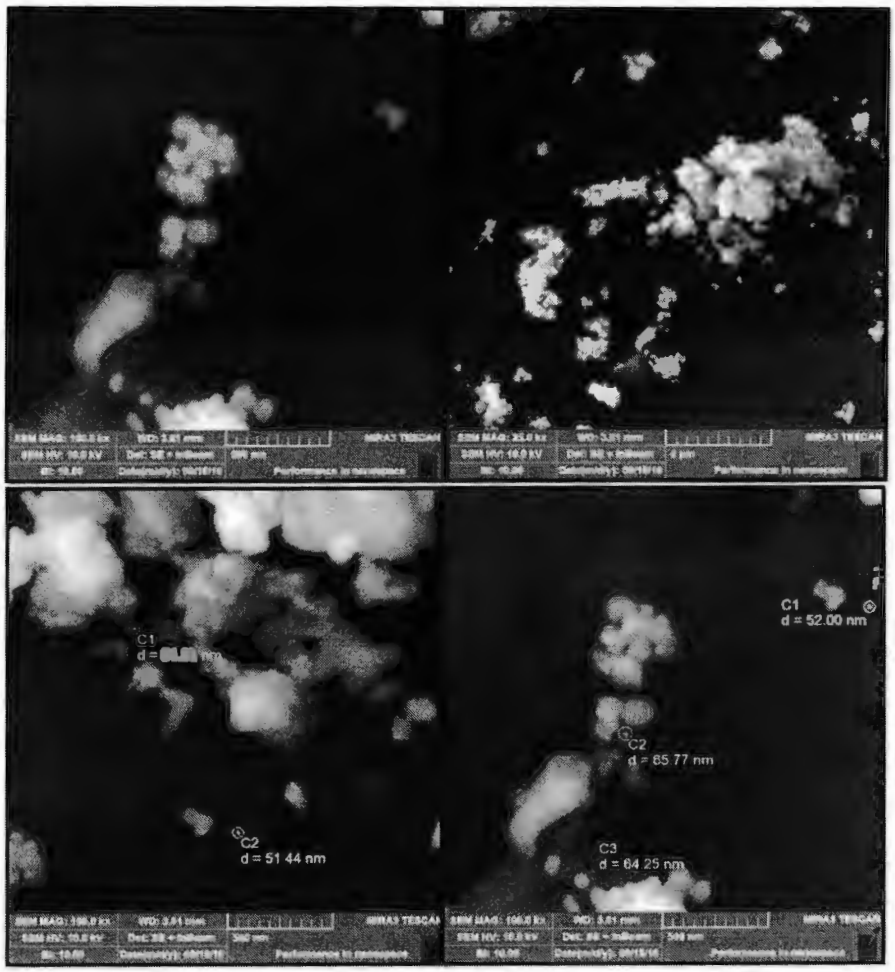

Figure 4.5: SEM micrograph of barium hexaferrites doped with x=0.04

Figure 4.6: SEM micrograph of barium hexaferrites doped with x=0.08

With increasing the doping concentration there is no evidence of change in shape of the particles. This can be attributed to change in the synthesis environment, handling of sample in autoclaves and reaction time. The hydrothermal synthesis is structure sensitive technique as our material is more sensitive to synthesis conditions as reported earlier [12]. Figure 4.7 shows the observed images of sample with$x = 0.1$

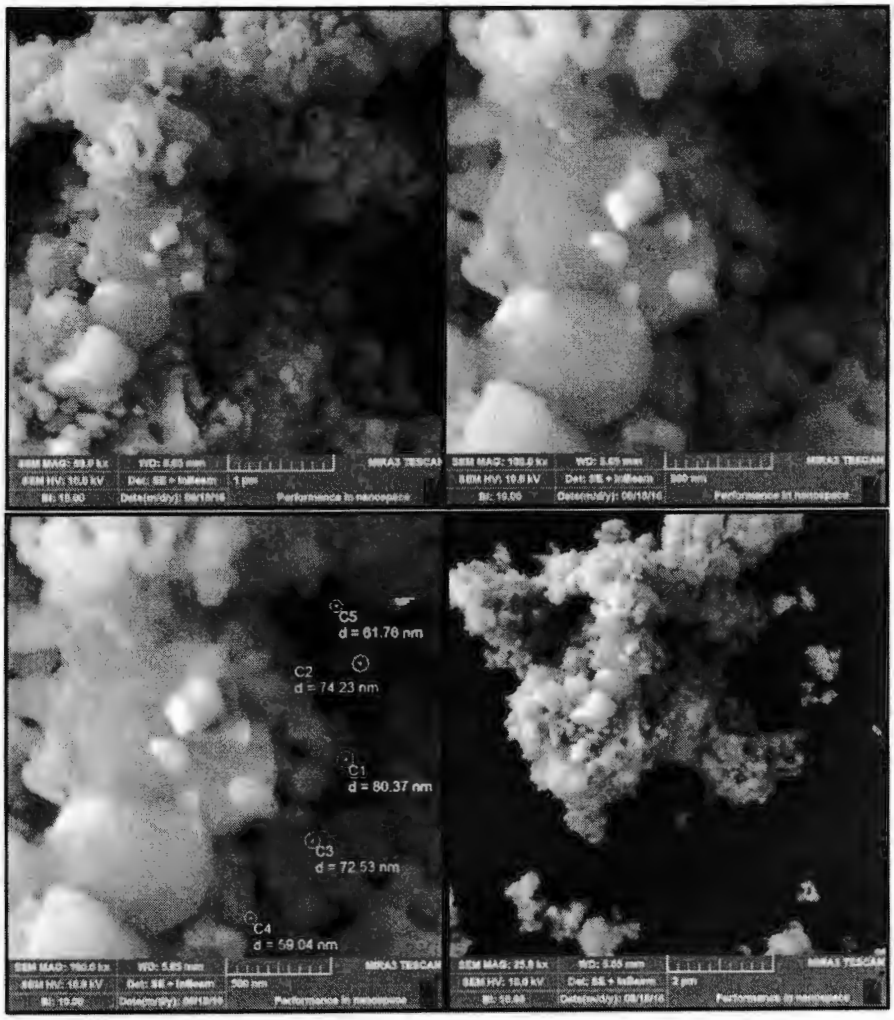

Figure 4.7: Observed SEM micrographs with x=0.1

4.3 Transmission electron microscopy

The TEM micrographs of the sample with x = 0.02, is shown in figure 4.8. The particle size is is found to be 55 nm. The structures visualized in the TEM micrographs reveal the individualed nanoparticles are assembled together in a continuous formation to form wire like structures which confirms the results observed in SEM earlier. The magnified image shows that the particles are spherical in shape, with size falling in range mentioned above.

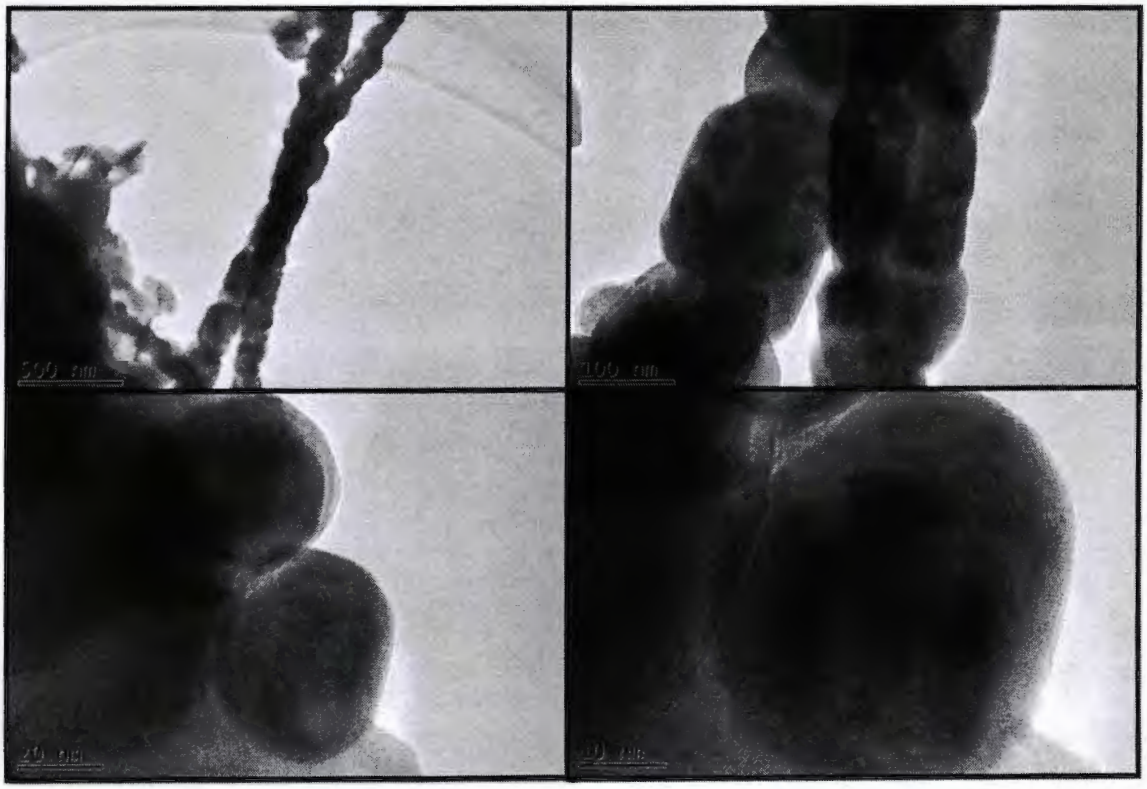

Figure 4.8: Morphology of sample x=0.02 demonstrated by TEM

The morphological investigation of the samples with $x = 0.04$ by TEM demonstrate the size 62nm. The images again show that the doped particles with concentration mentioned above show a sepherical or round-shape morphology. The critical diameter ofthe barium hexaferrite with single magnetic domin is reported to be less then 1μm [40] so, the prepared samples are single! domain. Figure 4.9 shows the particle formed with $x = 0.04$.

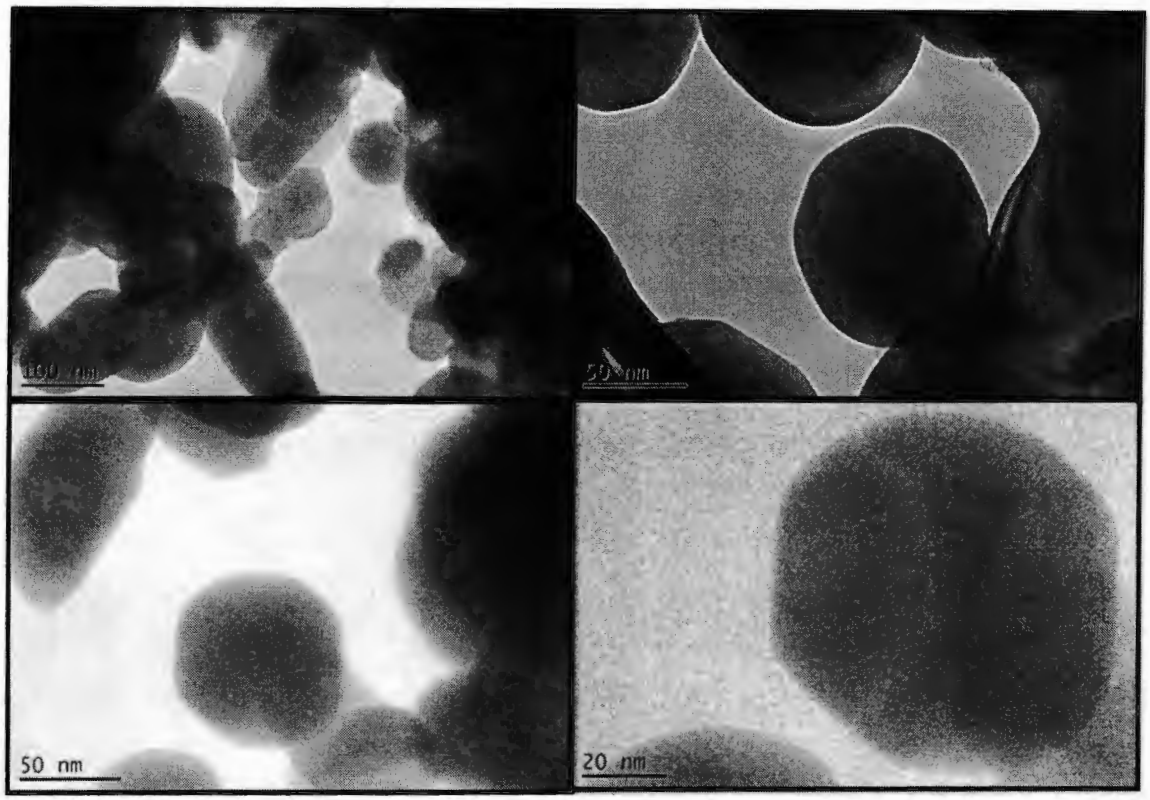

Figure 4.9: TEM micrograph of sample x=0.04

The images of sample x=0.08 and 0.1 also demonstrate same trend in shape of particles with different sizes. The size of sample with x=0.08 is calculated to be 25 nm. Figure 4.10 demonstrates the shape of nanoparticles formed. All of the mentioned size calculation was carried out through the scale and information provided through micrographs. The size varies in each sample and shows no particular trend with addition of Europium.

The sample with x=0.01 reveal the size of 102 nm. Figure 4.11 shows the formation of irregular spheres with some round shaped nanoparticles. There is no abrupt change in shape of the particles with doping or an increment in amount of dopant. It can be concluded on the basis of information provided through TEM that the dopant did not had a nominal effect in shape of the particles in the presented study. Difference in sizes of x=0.08 and 0.1 is observed in SEM and TEM results which point out the wide range of particles sizes in the sample.

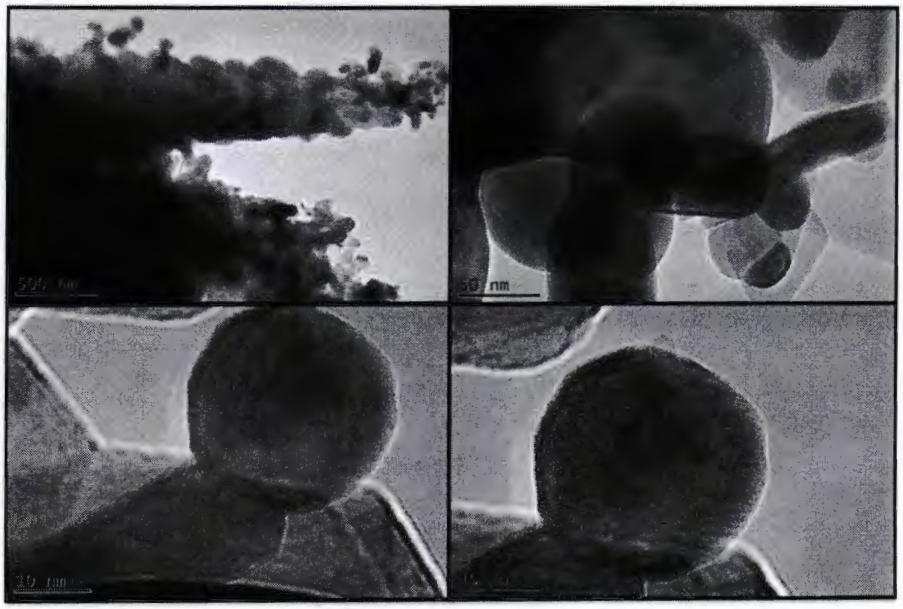

Figure 4.10: Observed TEM micrographs for x=0.08

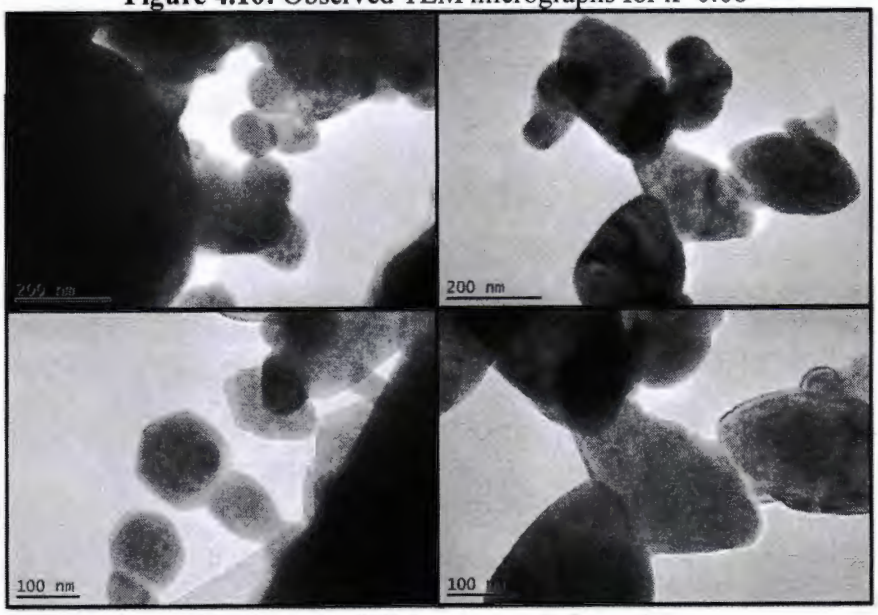

Figure 4.11: TEM micrograph for x=0.1

4.4 Energy dispersive X-ray spectroscopy

The energy dispersive X-ray spectroscopy reveals the elemental composition of material under investigation. Through EDS, weight percent and atomic percent of each element is also measured precisely which helps in recognition of impurities in material. The figure 4.12 shows EDS spectrum for un-doped sample, clearly indicating each peak with no impurities present in the material. Table 4.1 lists the elemental compositions in the material.

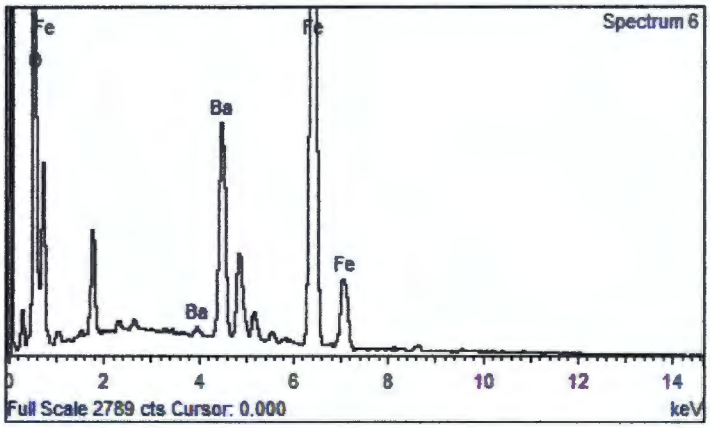

Figure 4.12: EDX spectrum for Un-doped $BaFe_{12}O_{19}$

Table 4.1: Concentration of elements in sample calculated by EDX

Element	Weight%	Atomic%
O K	25.45	59.62
Fe K	50.33	33.77
Ba L	24.21	6.61
Total	100.00	

The spectrum obtained for materials doped with concentrations x=0.02(a) and 0.04(b) are demonstrated in figure 4.13 below. The spectrum indicates peaks for each element present in the material. The peak of Europium appears in the spectrum and no additional peak of any other impurity was observed. The percentage of Europium present in the material is listed in the table 4.2 which increases with doping concentrations.

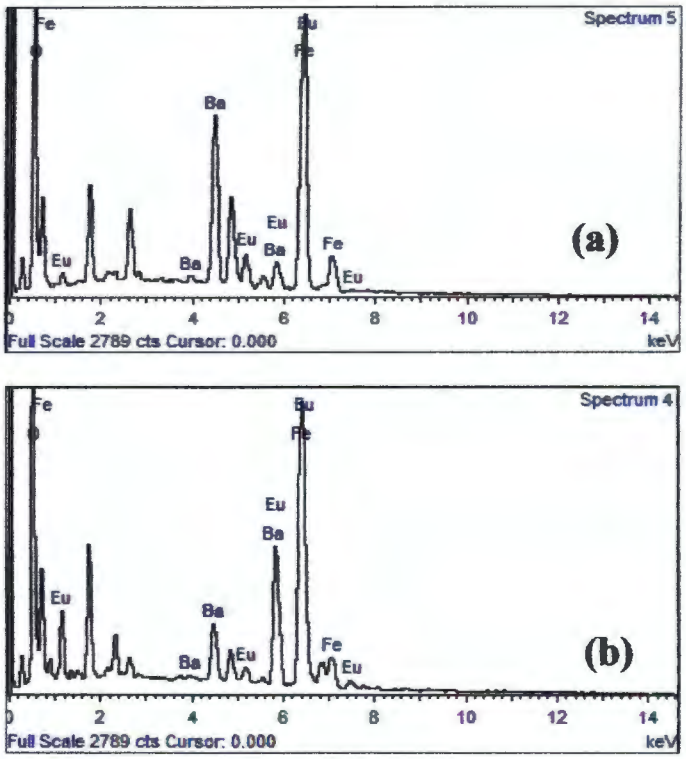

Figure 4.13: EDX spectrum of x=0.02 **(a)** and 0.04**(b)**

Similar results were obtained through EDS analysis of sample doped with x=0.08(c) and 0.1(d). The observed spectrum revealed that no impurity was present in prepared sample. Each element was identified through peaks present in the spectrum.

Table 4.2: Chemical composition of sample x=0.02 and 0.04

Element (x=0.02)	Weight%	Atomic%	Element (x=0.04)	Weight%	Atomic%
O K	22.82	59.81	O K	21.89	56.95
Fe K	37.78	28.36	Fe K	45.22	33.70
Ba L	32.92	10.05	Ba L	11.50	3.49
Eu L	6.47	1.79	Eu L	21.40	5.86
Totals	100.00		Totals	100.00	

The spectrum also demonstrates an increase in the Eu concentration with increased doping concentration. Concentrations of different elements are listed in table 4.2 for x=0.02 and 0.04. The observed spectrums for sample x=0.08 and 0.1 are shown in figure 4.13.

Table 4.3 shows the elemental composition of both the samples

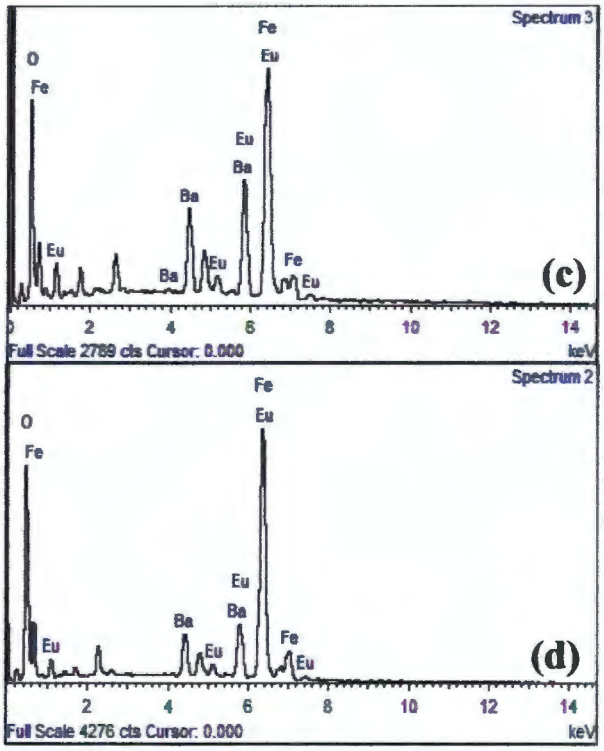

Figure 4.14: EDX spectrum for x=0.08(c) and 0.1(d)

Table 4.3: Concentration of elements in x=0.08 and 0.1 determined through EDX

Element x=0.08	Weight%	Atomic %	Element x=0.1	Weight%	Atomic%
O K	27.42	67.60	O K	17.64	55.37
Fe K	29.76	21.02	Fe K	29.52	26.54
Ba L	9.79	2.81	Ba L	17.84	6.52
Eu L	33.02	8.57	Eu L	35.00	11.56
Totals	100.00		Totals	100.00	Totals

4.5 FTIR analysis

The FTIR spectral study shows characteristics bands of each bond in different frequency ranges caused by molecular vibrations. The figure 4.15 illustrates the observed FTIR spectrum for un-doped and doped material. All the observed peaks fall in the finger print region of metal oxides.

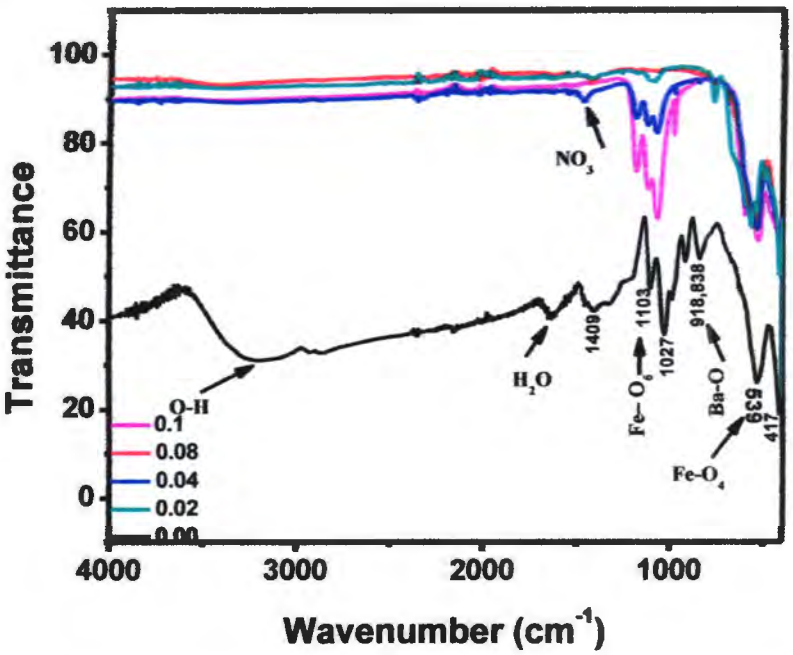

Figure 4.15: Observed FT-IR spectrum of $Eu_{1-x}Ba_xFe_{12}O_{19}$

FTIR spectra in figure 4.15 shows the absorption bands at417, 539, 848,918 and 1027 cm^{-1}which is a characteristic band range of metal oxides and shows successful formation of ferrites. The frequency band in the range 400–440 cm^{-1}iscaused by lattice vibrations of octahedral metal ions. The band at 1414 $cm^{-1}$is attributed to the characteristic band of NO^{-3}[23]. The samples show an absorption band from 3400-3000 related to hydrogen bonded O–H stretching. Presence of an absorption band centered at 1641 cm^{-1} also shows presence of water molecules in sample. The spectrum does not show any characteristic bond of europium. It can be seen from graph that there is no considerable change in band positions, which shows that lattice constant and Fe^{+3}–O^{2-}distances does not change by Eu doping.

4.6 Impedance spectroscopy

4.6.1 Impedance

The electrical properties of all the samples were measured with the impedance analyzer at room temperature. Figure 4.16 shows the plots for real and imaginary parts of impedance (Z' and Z") for un-doped sample. The plot reveals that the real part of impedance decreases with increasing frequency. This trend continues with increment in frequency. The real part (Z') of impedance is related to the resistance of the prepared sample. Imaginary part of impedance (Z") also decreases with an increase in frequency as indicated by the figure. This plot is suitable for the evaluation of the relaxation point in the material. In the un-doped material there are two relaxation points observed as there are peaks at two different points. The variation of impedance of the material with frequency suggests an increase in the conductivity with increased frequency, which is the behavior of metal oxides reported earlier

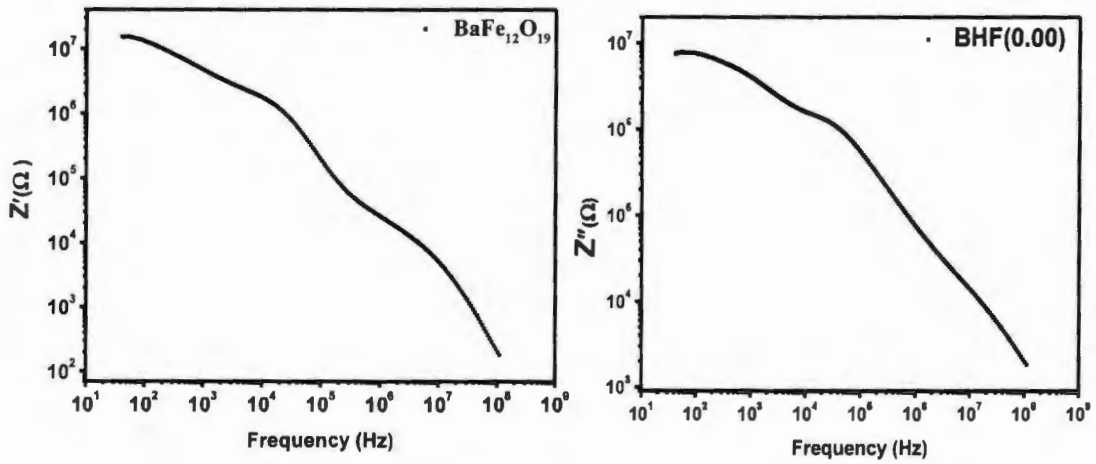

Figure 4.16: Plot for real (Z') and imaginary parts(Z") of $BaFe_{12}O_{19}$

The variation of Z' and Z"(real and imaginary part of impedance) with different doping concentrations (x= 0.02, 0.04, 0.08 0.1) is also analyzed by the impedance spectroscopy. The plot in figure 4.17shows that the real and imaginary parts of the impedance decrease with increase in frequency. Decrease in real part of impedance shows the conductive behavior of the doped sample as indicated in the pure sample.

When compared to the pure (un-doped) sample, doped samples show decrease in the impedance values. The impedance falls when the sample is doped with $x = 0.02, 0.04$ *and* 0.08 (Eu) at the lower frequencies. Which suggests that small amount of doping will have upbeat effect on the conductivity. As the doping concentration is increased further, the impedance rises again. This suggests that up to certain concentration the doping will have positive outcomes but further increase will have adverse effect on electrical properties. Increase in impedance values of sample 0.1 reveals that further increase in the doping will increase the resistance in material as well.

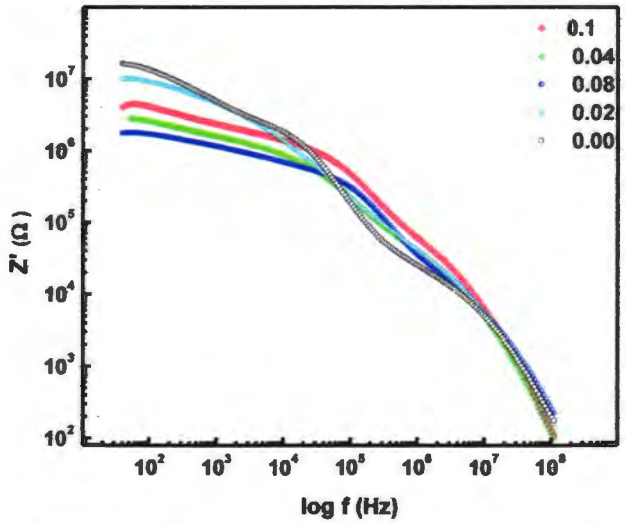

Figure 4.17: Plot for real part of impedance as a function of frequency

Between the ranges 10^5-10^7 Hz the resistance of the doped materials is greater than the pure sample and increases in each sample with doping. As the frequency increases, real part of impedance appears to merge irrespective of the doping concentrations. This effect suggests the possible release of the space charge and lowering of the barrier properties at higher frequencies [41]. The imaginary part of impedance explains the effects caused by doping on the relaxation points of the material. From the observed graph in figure 4.18 it can be seen that the relaxation points show a shift towards the higher frequency. This behavior shows promotion of short range ion mobilities in material with doping.

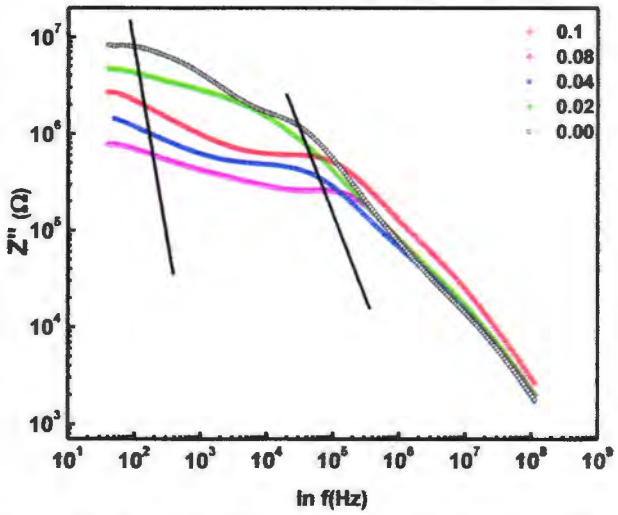

Figure 4.18: Imaginary part of impedance as a function of frequency for different doping concentrations

The loss spectrum (Z") can explain a number of important characteristics of materials such as:

a) The graph shows different relaxation points for each material due to different electro-active regions in each material.
b) The shifts in peaks of relaxation points can be explained on the terms of grain boundaries and broadening of the peaks shows the inhomogenity of the prepared samples.
c) The asymmetrical nature of the peaks are observed in the graph which suggests that our material shows non-Debye behavior [42, 62]

4.6.2 Dielectric constant (Ɛ') and dielectric loss factor (Ɛ")

The graph in Fig 4.19 shows the observed spectrum for the real (Ɛ') and imaginary part (Ɛ") dielectric constant of the un-doped M-type barium hexaferrites.

Dielectric constant can be described as the ability of the medium to resist the flow of charge. According to the measurements, the dielectric constant of material decreases with increase in the frequency.

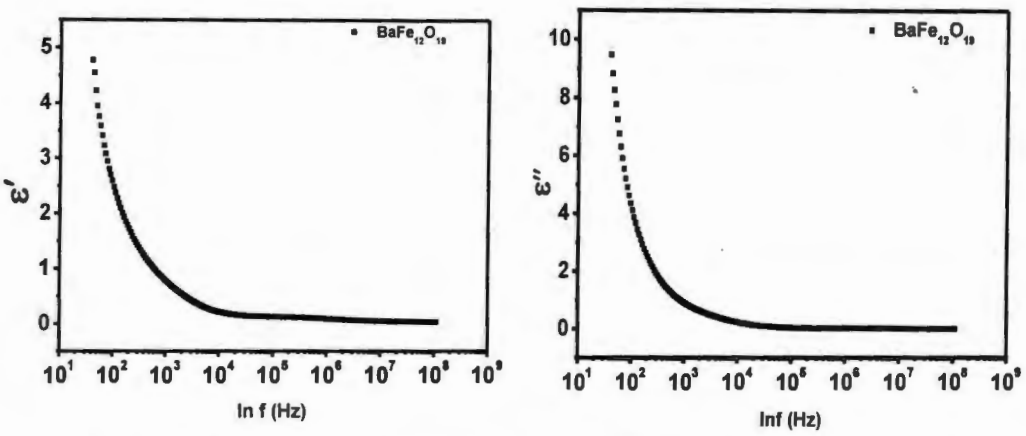

Figure 4.19: Plot for dielectric constant (Ɛ') and dielectric loss factor (Ɛ") for $BaFe_{12}O_{19}$

Dielectric behavior of the ferrites can be explained on the basis of Maxwell-Wagner two layers model. According to this model first layer is made of large number of grains, acting as conductive layer at lower frequencies and second layer is composed of grain boundaries which are highly conductive at high frequencies. The mechanism followed for conduction and polarization in ferrites is same i.e. hopping. The electrons hop between Fe^{2+} and Fe^{3+} ions to polarize the material. When the frequency increases, it is difficult for the electron to hop between ferrous and ferric ions with the frequency alternations. This reduces the possibility of electrons to reach the grain boundary. It causes the net displacement of charge to decrease in one direction. Consequently the dielectric constant decreases[24].

The dielectric loss factor Ɛ" also shows decrease with increase in the frequency values. As discussed earlier when the frequency increases the dielectric constant decreases which causes the loss factor (Ɛ") to decrease with frequency. At lower frequencies, the high dielectric loss factor can be a result of crystal defects and moisture in the material.

The plots for dielectric constant and dielectric loss factor for different doping concentrations are shown in figure 4.18. According to the graphs, the dielectric constant of the doped material follows same trend as in un-doped material with respect to frequency i.e. decrease in dielectric constant by increasing the frequency.

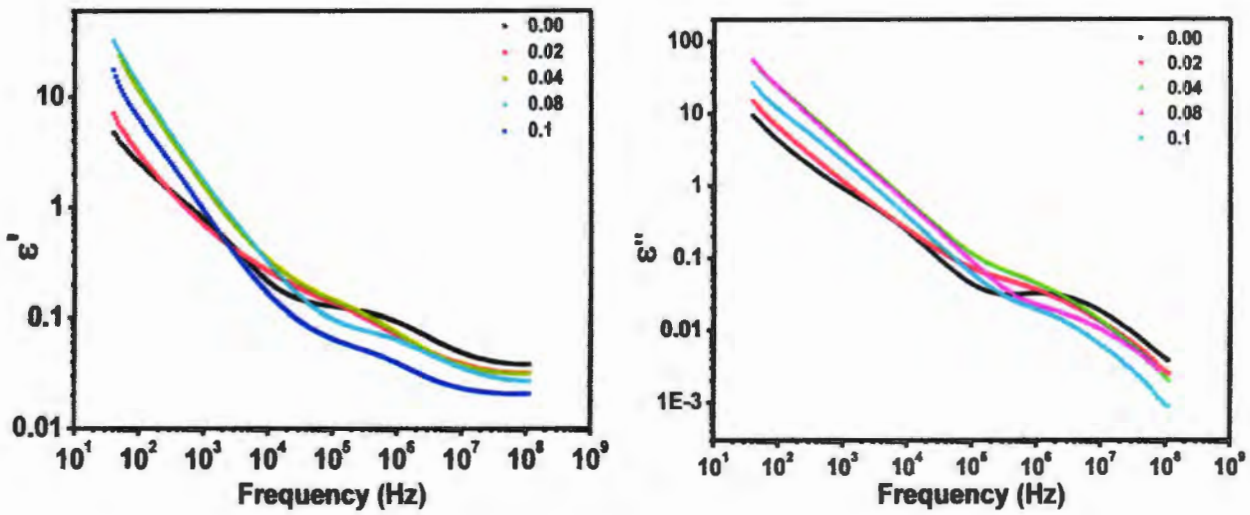

Figure 4.20: Plot for dielectric constant (Ɛ') and dielectric loss factor(Ɛ") with different doping concentrations

Increase in dielectric properties with increase in grain size in ceramic materials was also reported earlier[63, 64]. Our material shows increase in grain size with doping which causes increase in dielectric constant based on ferroelectric behavior of ferrites reported earlier [64, 65].

In a ferroelectric material, the single crystal often has multiple domains. These domains are separated by interfaces called domain walls. The mobility of domain walls and the population of domains in the materials affect the dielectric constant. As the grain size increases, the domain walls are free to move and the grain boundaries contribute as an additional pinning point to moving walls. The movement of domain walls provides transition between different dipole alignments which increases the dielectric constant.

4.6.3 Electric modulus analysis

The electric modulus of ionic materials helps to analyze the space charge relaxation phenomena in the material. It is now widely used to analyze the behavior of electrical conductivities of the material as well. The real (M') and imaginary part (M") of the electric modulus are shown in figure 4.21.

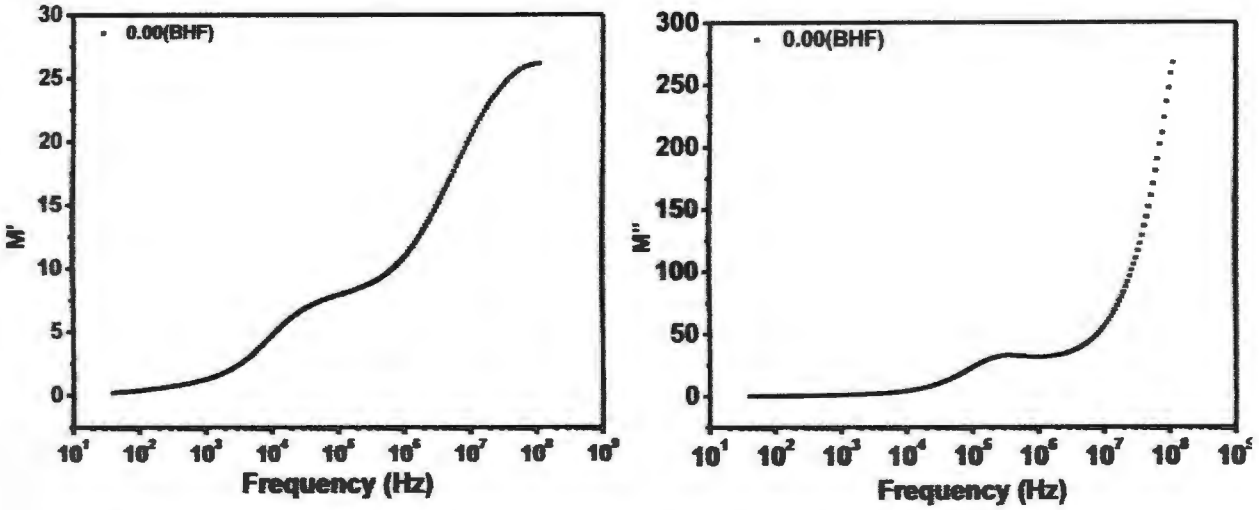

Figure 4.21: Plot for real (M') and imaginary part (M") of electric modulus of $BaFe_{12}O_{19}$

Two relaxation points are observed in the material at lower and higher frequencies respectively. The electric modulus of the material increases with increasing frequency which is the opposite of dielectric behavior. This trend predicts the increase in the conductivity with increasing frequency which is the behavior of material reported earlier. The behavior of electric modulus with doping concentration is shown in figure 4.22. According to the observed spectrum, the real and imaginary parts of the electric modulus increase with increase in frequency in each sample.

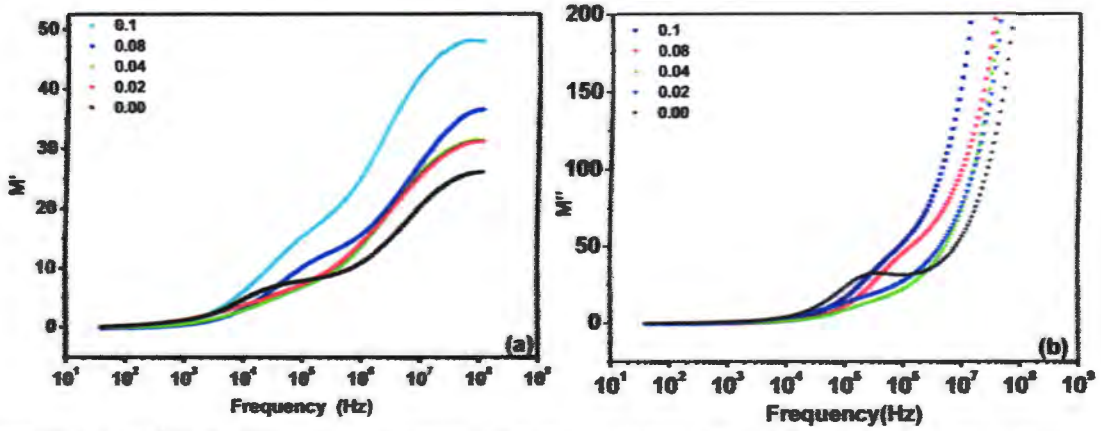

Figure 4.22: Real (a) and imaginary (b) parts of electric modulus with different doping concentrations(x)

The figures reveal that for lower frequency ranges, real and imaginary parts of modulus decrease for samples $x = 0.02, 0.4$ and 0.08 as compared to un-doped samples. This predicts more conductive behavior for the doped samples at lower frequencies. As the frequency increases, the electric modulus also increases and the space charge relaxation points shift to the higher frequencies with increase in doping of the material (Eu) in the imaginary part of modulus (b). These peaks show the transition from long range to short range mobility with increasing frequency. The low frequency side of the peak represents the range of frequencies in which the ions can have long distance transitions i.e. hopping form one site to another and for the high frequency ranges the ions are confined spatially and can execute only localized motions.

4.6.4 Tangent loss

The graph in figure 4.23 shows the spectrum for tangent loss values of barium hexaferrites. The tangent loss decreases in the material with increase in frequency. The tangent losses can be explained in term of conduction losses in the material. The conduction losses depend on the concentration of Fe^{2+} ions on 2k sites at lower frequency regions there is more dispersion of charges as compared to high frequency region. This can be explained on the fact that at lower frequencies more time is available for the displacement of charges and the conductivity inside the grain is high and higher will be dielectric losses.

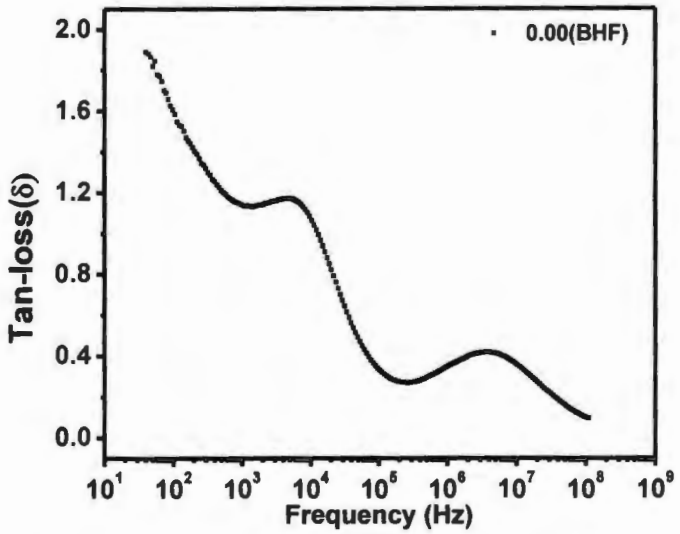

Figure 4.23: Tangent loss spectrum for $BaFe_{12}O_{19}$ as a function of frequency

As the frequency is increased, the hopping of charge carriers cannot follow the applied frequency which decreases the conduction inside the grain hence the tangent loss is decreased. The figure also shows prominent relaxation peaks with increasing frequency. These peaks are observed when the hopping frequency of the charge carriers becomes approximately equal to that of the applied electric field, it causes resonance and results in the appearance of relaxation peaks [66]. Variation of tangent loss with composition can be observed in figure 4.24. The figure shows that with increasing the doping in the material, the tangent loss increases in each sample.

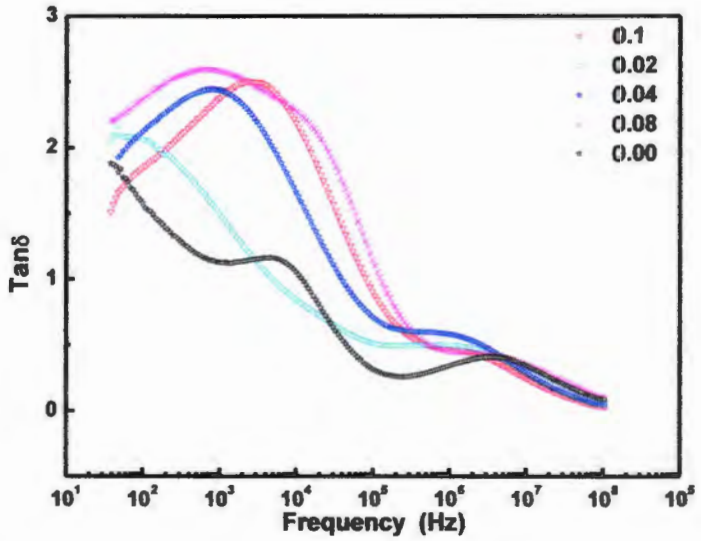

Figure 4.24: Plot for tangent loss with different doping concentrations

For the composition $x = 0.1$ the dielectricloss starts to decrease with composition. Decrease in tangent loss can be due to decrease in the dielectric constant.

4.6.5 AC conductivity

The variation of AC electrical conductivity is demonstrated by plot shown in figure 4.25. The plot reveals that with increasing the frequency, ac conductivity of material increases. In case of ionic solid the conduction is because of movement of ions and depends on angular frequency. Increase in the ac conductivity with frequency can be explained on the pumping force of the applied electric field which effects the migration of charge carriers between localized states. This pumping force also liberates the conducting charge carriers from different areas that experience hindrance by material and act as trapping centers. Increase in the frequency increases the

hopping frequency of electrons between the charge carriers which results increase in the conduction. Maxwell-Wagner model explains the conduction process successfully. According to proposed two layer model dielectric material have a two layer structure, i.e. grains separated by poorly conducting grains. At lower frequencies grain boundaries are much active and the hopping frequency of electron between the Fe^{3+} and Fe^{2+} is less

As the frequency is increased the conductive grain layers become much active in keeping hopping of electrons. This effect causes the hopping frequency to increase thereby increasing the

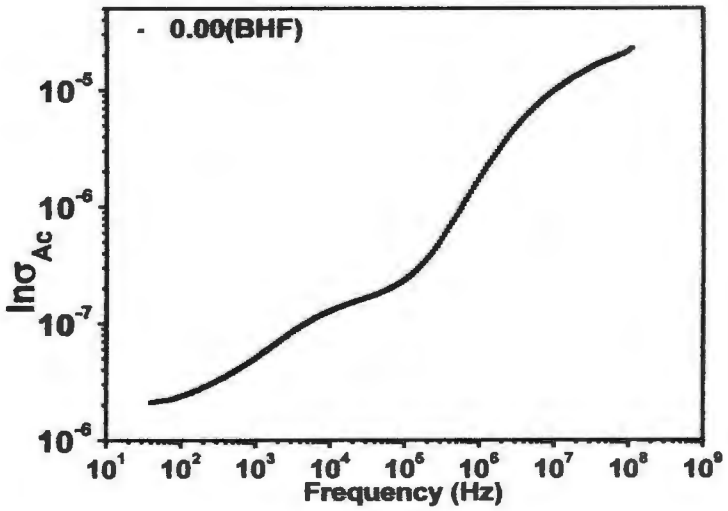

Figure 4.25: Conductivity spectrum for $BaFe_{12}O_{19}$as a function of frequency

AC conductivity. The figure 4.26 shows the plot of AC conductivity of different doping concentrations with frequency. It can be seen in the figure that conductivity of each sample decreases when compared to un-doped sample at higher frequencies however, doped material follows the trend of increase in conductivity with frequency. At the lower frequency range the doped samples show an increase in the conductivity as compared to pure barium hexaferrites. The graph shows that for lower frequency, the conductivity increases with increase in doping composition. But as the doping concentration increases from x=0.08 to 0.1, the conductivity decreases at high frequencies. This suggests that further increment in doping concentration will have unfavorable effect on conductivity. The result is in well correspondence with the earlier explained results.

The conduction in $BaFe_{12}O_{19}$ is mainly due to hopping of electron between Fe^{3+} and Fe^{2+} as explained earlier. It has been observed that substitution of rare earth ions in Sr^{2+} or Ba^{2+} ions tends to change the Fe^{2+} and Fe^{3+} which leads an increase in conductivity of $BaFe_{12}O_{19}$ [67]. The high frequency regions show decrease in the conductivity with increase in doping concentrations. This suggests that Eu-doped barium hexaferrites show best results in conductivity at low frequency. At high frequency, the decrease in conductivity can be attributed to increase in grain size gradually. The contribution due to grains in conductivity decreases with high frequency. All conductive contributions are due to surface of the grain as the frequency alternations are high.

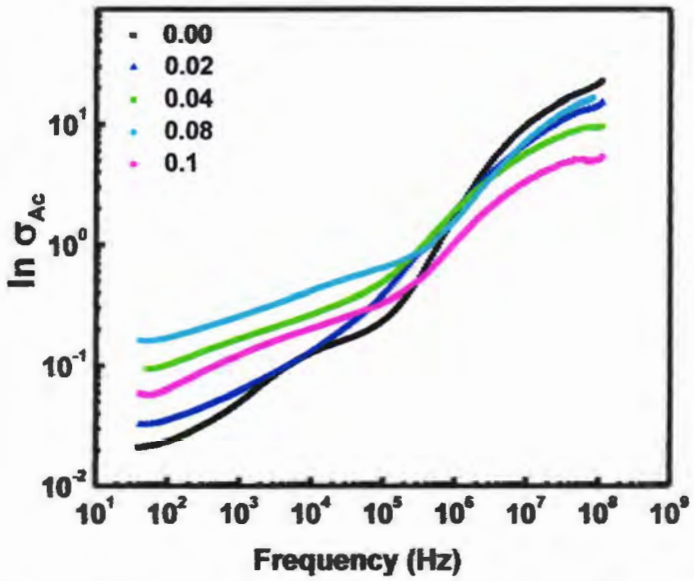

Figure 4.26: Plot for Ac conductivity as a function of frequency with different compositions

4.6.6 Nyquist Plot

The figure 4.27 shows the Nyquist plot for the studied samples. It can be seen that the material exhibit two semicircles for the un-doped and doped material as well. The electrical circuit which describes this behavior is a series combination of two circuits with a resistor and a constant phase element in parallel. The small diameter of semicircle at high frequency of all the samples indicates low resistance. The diameter of the semicircles decreases with doping concentrations which indicates decrease in the resistance. In the Nyquist plot, the semicircles are generally described by the grain (bulk) and grain boundaries (interface) effects. At low frequency regions,

grain boundary resistance is observed while grain effect appears at high frequency. Small diameter of the semicircle at higher frequencies indicates small resistance. The frequency tends to increase from right to left. The resistance and capacitance of interfacial grain boundary is normally. The parameters R_g (grain resistance) and R_{gb} (grain boundary resistance) were determined for all doping concentrations using the Z-view software. The solid line in the figure indicates the fitted data Equivalent circuit used to fit the electrical data of samples can be seen in figure 4.28.

The values of resistance due to grains (R_g) and grain boundaries (R_{gb}) are summarized in the table for each sample in the present study. It is evident from the values as well as Nyquist plot that contribution of grain resistance is increasing in the material with increase in the doping concentration and resistance due to grain boundaries is decreasing.

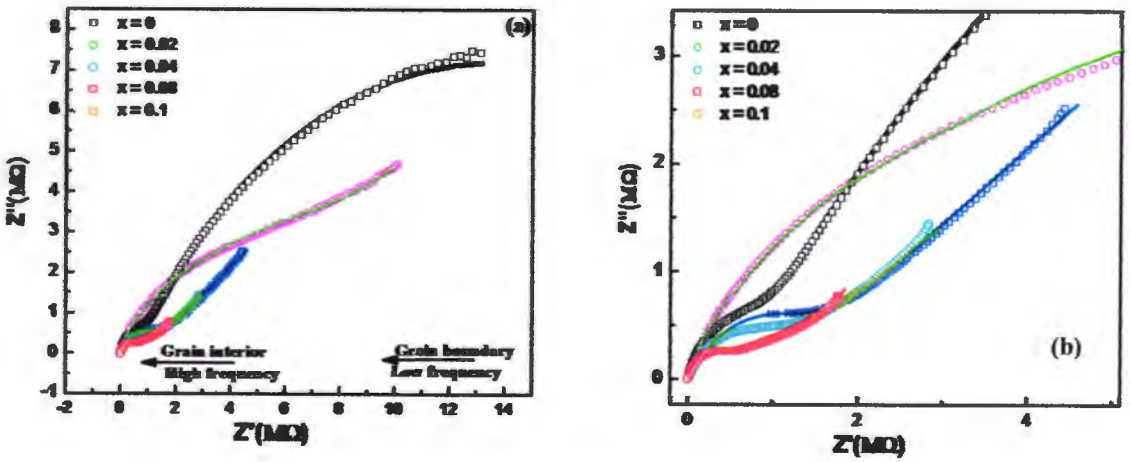

Figure 4.27: (a) Nyquist plot of the investigated samples(b) magnified plot

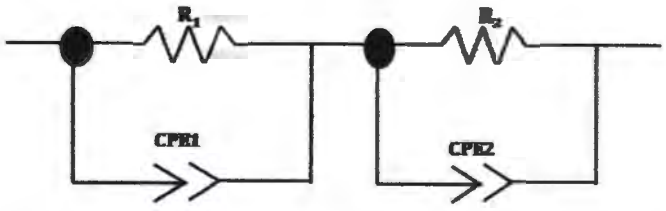

Figure 4.28: Equivalent circuit used to fit the electrical data of samples

The increase in Rg can be explained on the fact that the grain size is increasing with doping which increases the resistance contribution. The value of n determines the divergence from ideal Debye behavior, and its value is 1 for pure capacitor and zero for pure resistor[68].

Table 4.4: Extracted parameters at all doping concentrations from fitting

Composition(x)	$R_g(\Omega)$	C_g(nF)	n_g	$R_{gb}(\Omega)$	C_{gb}(nF)	n_{gb}
0	609730	7.28×10^{-12}	0.98	2.5898×10^{-12}	1.01×10^{-9}	0.64
0.02	7.5×10^{6}	5.7×10^{-8}	0.67	7.5×10^{6}	6.0×10^{-7}	0.95
0.04	1.6×10^{7}	3.6×10^{-6}	0.45	1×10^{6}	8.7×10^{-7}	0.69
0.08	6.0×10^{7}	2.4×10^{-7}	0.5	5.00×10^{5}	2.0×10^{-6}	0.47
0.1	1.9×10^{8}	4.7×10^{-7}	0.41	1.0911×10^{6}	2.16×10^{-8}	0.76

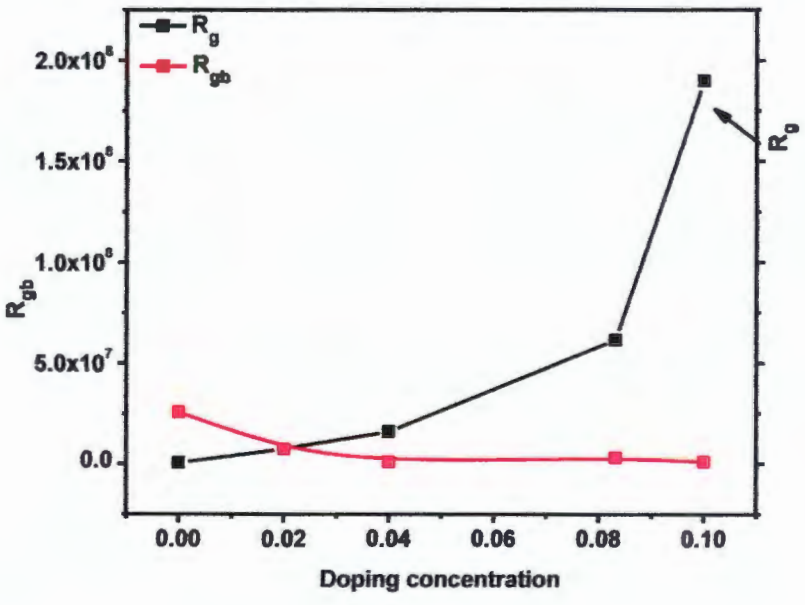

Figure 4.29: Plot of resistance due to grain and grain boundaries as a function of doping concentration(x)

4.7 Magnetic properties

4.7.1 Hysteresis curve

The hysteresis curve for all the prepared samples is shown in figure 4.30. The values of Ms, Mr and coercivity are calculated from the hysteresis loop. The figures 4.30 and 4.31 clearly reveal increase in saturation magnetization with doping concentrations.

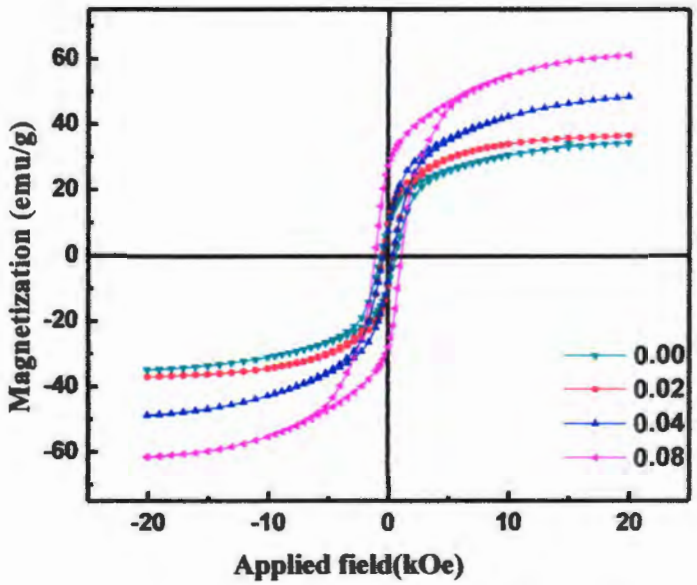

Figure 4.30: Observed hysteresis Curve for different doping concentrations in $BaFe_{12}O_{19}$

The values of M_s and H_c are summarized in table 4.5. The increase in M_s can be explained on the fact that it depends upon Fe^{3+}–O–Fe^{2+} super-exchange interactions. It has been observed that the substitutions of rare earth metal ions with Sr^{2+} and Ba^{2+} in M-type hexaferrites causes a change in valence states of Fe^{3+}ions to Fe^{2+}ions at 2a sites[40]. As result the super-exchange interaction between Fe^{3+}–O–Fe^{2+} increases. The enhancement in super-exchange interaction causes the hyperfine field to increase at 12k and 2b sites which increases the saturation magnetization. The materials with high saturation magnetization are required in the high density recording media as reported earlier [69, 70]

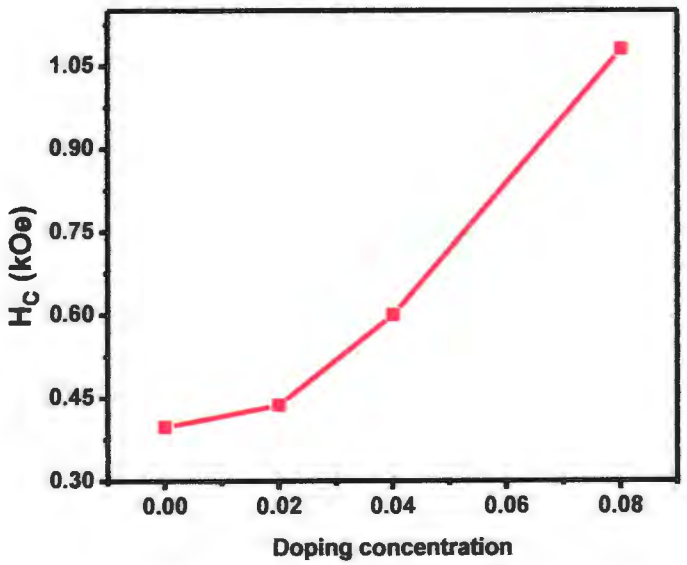

Figure 4.32: Variation of H_c as a function of doping concentration (x)

Chapter 5

Conclusions and Future Recommendations

Hydrothermal technique was employed to prepare pure and doped $BaFe_{12}O_{19}$ nanoparticles. Doping concentrations of Europium (Eu^{3+}) was varied from 0.02 to 1 in $BaFe_{12}O_{19}$. XRD analysis showed the single phase of doped and un-doped material which demonstrated the purity of sample. SEM and TEM analysis were used to reveal the morphology and size of prepared samples. SEM images showed that the particles were spherical in shape and size of particles was increasing with the doping concentrations (24.9-102nm). Analysis of the un-doped material through SEM revealed the mixture of disks and spherical shaped structures. EDX spectrum confirmed the purity of sample and elemental composition was observed to be same like the stoichiometric ratio of the starting chemicals.

Impedance spectroscopy was employed in the frequency range 20Hz to 2Mz to examine the electrical properties of doped and undoped$BaFe_{12}O_{19}$nanoparticles. At low frequency, the dielectric constant was observed to increase with doping indicating enhanced conductive behavior while at high frequency region; dielectric constant tends to merge indicating release of space charges. Two relaxation points appeared in electric modulus spectrum and revealed increase in values with increase in frequency. The Ac conductivity of prepared samples also exhibited similar transitions. With increase in doping, the conductivity of each sample increased as a function of frequency. At the lower frequency region, the conductivity increased with doping while at higher frequency the conductivity was decreased. Two semicircular arcs were determined in the complex impedance plane attributed to different relaxation times in system at different frequency regions. The semicircle at the high frequencies was attributed to grains and the semicircle at higher lower frequencies was distinctive due to grain boundaries. The radius of semicircles is related to R_g and R_{gb}. Resistance due to grains was increased in each sample with doping concentration while resistance due to grain boundaries was decreased. The experimental data was fitted with a model of equivalent RC circuit consisting of a resistor in parallel and constant phase element in series with the help of Z-view software. This helped in separation of the contribution to conductivity due to grains and grain boundaries.

The magnetic properties of the prepared material were characterized by VSM. The saturation magnetization and coercivity was increased with increasing the doping concentration. With the addition of rare earth ions, super-exchange interaction between Fe^{3+}–O–Fe^{2+} increased in the material caused by change in valence states of Fe^{3+}ions to Fe^{2+}. The increase in coercivity is caused by increase in magnetocrystalline anisotropy of material through doping.

5.1 Future recommendations

The material studied during this work shows high saturation magnetization which makes it suitable for high frequency devices. The potential applications of barium hexaferrites can be investigated for application in microwave devices as our material indicated increase in resistivity at high frequency with doping concentrations. The high resistivity with low magnetic losses enables low insertion losses in microwave devices.

It has been observed during study that the doping concentrations improve the electrical properties up to certain concentration (0.08) and then starts to decrease with further increase. This effect can be studied in detail with their potential applications.

References

[1] J. Smith, H. Wijn, Ferrites, Eindhoven: Philips' Technical Library, (1959).

[2] X. Liu, P. Hernández-Gómez, Y. Deng, K. Huang, X. Xu, S. Qiu, D. Zhou, Analysis of magnetic disaccommodation in La 3+–Co 2+-substituted strontium ferrites, Journal of Magnetism and Magnetic Materials, 321 (2009) 2421-2424.

[3] L. Gama, A. Diniz, A. Costa, S. Rezende, A. Azevedo, D. Cornejo, Magnetic properties of nanocrystalline Ni–Zn ferrites doped with samarium, Physica B: Condensed Matter, 384 (2006) 97-99.

[4] A.B. Gadkari, T.J. Shinde, P.N. Vasambekar, Magnetic properties of rare earth ion (Sm 3+) added nanocrystalline Mg–Cd ferrites, prepared by oxalate co-precipitation method, Journal of Magnetism and Magnetic Materials, 322 (2010) 3823-3827.

[5] T. Nakamura, T. Miyamoto, Y. Yamada, Complex permeability spectra of polycrystalline Li–Zn ferrite and application to EM-wave absorber, Journal of magnetism and magnetic materials, 256 (2003) 340-347.

[6] X. Liu, B. Cheng, J. Hu, H. Qin, M. Jiang, Semiconducting gas sensor for ethanol based on $LaMg_x Fe_{1-x} O_3$ nanocrystals, Sensors and Actuators B: Chemical, 129 (2008) 53-58.

[7] A. Gadkari, T. Shinde, P. Vasambekar, Structural analysis of Y^{3+}-doped Mg–Cd ferrites prepared by oxalate co-precipitation method, Materials Chemistry and Physics, 114 (2009) 505-510.

[8] D.F. Shriver, P.W. Atkins, C.H. Langford, Inorganic Chemistry, W.H. Freeman, 1994.

[9] L. Lechevallier, J. Le Breton, A. Morel, P. Tenaud, On the solubility of rare earths in M-type $SrFe_{12}O_{19}$ hexaferrite compounds, Journal of Physics: Condensed Matter, 20 (2008) 175203.

[10] S. Rösler, P. Wartewig, H. Langbein, Synthesis and characterization of hexagonal ferrites $BaFe_{12-2x}Zn_xTi_xO_{19}$ ($0 \leq x \leq 2$) by thermal decomposition of freeze-dried precursors, Crystal Research and Technology, 38 (2003) 927-934.

[11] R. Valenzuela, Magnetic ceramics, Cambridge University Press, 2005.

[12] J. Li, T.M. Gür, R. Sinclair, S.S. Rosenblum, H. Hayashi, Thermochemical stability of $BaFe_{12}O_{19}$ and $BaFe_2O_4$ and phase relations in the Ba-Fe-O ternary system, Journal of materials research, 9 (1994) 1499-1512.

[13] K.H.J. Buschow, F.R. Boer, Physics of magnetism and magnetic materials, Springer, 2003.

[14] G. Rangarajan, Materials science, Tata McGraw-Hill Education, 2004.

[15] A. Goldman, Modern ferrite technology, Springer Science & Business Media, 2006.

[16] P.W. Anderson, New approach to the theory of superexchange interactions, Physical Review, 115 (1959) 2.

[17] J.R.M. E. Barsoukov, Impedance Spectroscopy Theory, Experiment and Applicaions in, John Wiley and sons Inc., Hoboken, New jersy, 2005.

[18] M.J. Iqbal, S. Farooq, Extraordinary role of Ce–Ni elements on the electrical and magnetic properties of Sr–Ba M-type hexaferrites, Materials Research Bulletin, 44 (2009) 2050-2055.

[19] E. Verwey, P. Haayman, F. Romeijn, Physical properties and cation arrangement of oxides with spinel structures II. Electronic conductivity, The Journal of Chemical Physics, 15 (1947) 181-187.

[20] A. Aziz, E. Ahmed, M.N. Ashiq, M.A. Khan, N. Karamat, I. Ali, Structural, electrical, dielectric and magnetic properties of Mn-Nd substituted CoFeO 3 nano sized multiferroics, Progress in Natural Science: Materials International, 26 (2016) 325-333.

[21] H. Ikuta, K. Takanaka, M. Wakihara, The effect of chromium substitution on the phase transition of lithium manganese spinel oxides, Thermochimica acta, 414 (2004) 227-232.

[22] R.M. Almeida, W. Paraguassu, D.S. Pires, R.R. Correa, C.W. de Araujo Paschoal, Impedance spectroscopy analysis of BaFe 12 O 19 M-type hexaferrite obtained by ceramic method, Ceramics International, 35 (2009) 2443-2447.

[23] K.C. Kao, Dielectric phenomena in solids, Academic press, 2004.

[24] V.P. Singh, G. Kumar, P. Dhiman, R. Kotnala, J. Shah, K.M. Batoo, M. Singh, Structural, dielectric and magnetic properties of nanocrystalline BaFe12O19 hexaferrite processed via sol-gel technique, Adv. Mater. Lett, 5 (2014) 447-452.

[25] R. Tang, C. Jiang, J. Jian, Y. Liang, X. Zhang, H. Wang, H. Yang, Impedance spectroscopy and scaling behaviors of Sr3Co2Fe24O41 hexaferrite, Applied Physics Letters, 106 (2015) 022902.

[26] M.F. Din, I. Ahmad, M. Ahmad, M. Farid, M.A. Iqbal, G. Murtaza, M.N. Akhtar, I. Shakir, M.F. Warsi, M.A. Khan, Influence of Cd substitution on structural, electrical and magnetic properties of M-type barium hexaferrites co-precipitated nanomaterials, Journal of Alloys and Compounds, 584 (2014) 646-651.

[27] K.K. Mallick, P. Shepherd, R.J. Green, Dielectric properties of M-type barium hexaferrite prepared by co-precipitation, Journal of the European Ceramic Society, 27 (2007) 2045-2052.

[28] M. Radwan, M. Rashad, M. Hessien, Synthesis and characterization of barium hexaferrite nanoparticles, Journal of Materials Processing Technology, 181 (2007) 106-109.

[29] S. Che, J. Wang, Q. Chen, Soft magnetic nanoparticles of BaFe12O19 fabricated under mild conditions, Journal of Physics: Condensed Matter, 15 (2003) L335.

[30] H.M. Khan, M. Islam, Y. Xu, M.N. Ashiq, I. Ali, M.A. Iqbal, M. Ishaque, Structural and magnetic properties of Pr–Ni substituted Ca 0.5 Ba 0.5 Fe 12 O 19 hexa-ferrite nanoparticles, Ceramics International, 40 (2014) 6487-6493.

[31] Z.F. Zi, Q.C. Liu, J.M. Dai, Y.P. Sun, Effects of Ce–Co substitution on the magnetic properties of M-type barium hexaferrites, Solid State Communications, 152 (2012) 894-897.

[32] X. Batlle, X. Obradors, J. Rodríguez-Carvajal, M. Pernet, M. Cabanas, M. Vallet, Cation distribution and intrinsic magnetic properties of Co-Ti-doped M-type barium ferrite, Journal of applied physics, 70 (1991) 1614-1623.

[33] S. Jacobo, C. Domingo-Pascual, R. Rodriguez-Clemente, M. Blesa, Synthesis of ultrafine particles of barium ferrite by chemical coprecipitation, Journal of materials science, 32 (1997) 1025-1028.

[34] S. Nasir, A. Saleemi, M. Anis-ur-Rehman, Enhancement in dielectric and magnetic properties of Ni–Zn ferrites prepared by sol–gel method, Journal of Alloys and Compounds, 572 (2013) 170-174.

[35] K.K. Mallick, P. Shepherd, R.J. Green, Magnetic properties of cobalt substituted M-type barium hexaferrite prepared by co-precipitation, Journal of Magnetism and Magnetic Materials, 312 (2007) 418-429.

[36] F.M.M. Pereira, C. Junior, M.R.P. Santos, R.S.T.M. Sohn, F.N.A. Freire, J.M. Sasaki, J. De Paiva, A.S.B. Sombra, Structural and dielectric spectroscopy studies of the M-type barium strontium hexaferrite alloys (Ba x Sr1− x Fe12O19), Journal of Materials Science: Materials in Electronics, 19 (2008) 627-638.

[37] M.C. Dimri, S.C. Kashyap, D. Dube, Electrical and magnetic properties of barium hexaferrite nanoparticles prepared by citrate precursor method, Ceramics international, 30 (2004) 1623-1626.

[38] S. Abbas, R. Chatterjee, A. Dixit, A. Kumar, T. Goel, Electromagnetic and microwave absorption properties of (Co2+-Si4+) substituted barium hexaferrites and its polymer composite, Journal of applied physics, 101 (2007) 74105-74105.

[39] D. Lisjak, M. Drofenik, The low-temperature formation of barium hexaferrites, Journal of the European Ceramic Society, 26 (2006) 3681-3686.

[40] F. Khademi, A. Poorbafrani, P. Kameli, H. Salamati, Structural, magnetic and microwave properties of Eu-doped barium hexaferrite powders, Journal of superconductivity and novel magnetism, 25 (2012) 525-531.

[41] M. Costa, G.P. Júnior, A. Sombra, Dielectric and impedance properties' studies of the of lead doped (PbO)-Co 2 Y type hexaferrite (Ba 2 Co 2 Fe 12 O 22 (Co 2 Y)), Materials Chemistry and Physics, 123 (2010) 35-39.

[42] K. Hayat, M. Nadeem, M.J. Iqbal, M. Rafiq, M. Hasan, Analysis of electro-active regions and conductivity of BaMnO3 ceramic by impedance spectroscopy, Applied Physics A, 115 (2014) 1281-1289.

[43] A. Singh, S.B. Narang, K. Singh, O. Pandey, R. Kotnala, Electrical and magnetic properties of rare earth substituted strontium hexaferrites, Journal of ceramic processing research, 11 (2010) 241-249.

[44] C. Giacovazzo, Fundamentals of crystallography, Oxford University Press, USA, 2002.

[45] R. Guinebretière, X-ray diffraction by polycrystalline materials, John Wiley & Sons, 2013.

[46] R.F. Egerton, Physical principles of electron microscopy: an introduction to TEM, SEM, and AEM, Springer Science & Business Media, 2006.

[47] B. Hafner, Energy Dispersive Spectroscopy on the SEM: a primer, Citing internet sources http://www. charfac. umn. edu/instruments/eds_on_sem_primer. pdf, (2006).

[48] H. Ma, K.-J. Shieh, T.X. Qiao, S. Cherng, Transmission Electron Microscopy (TEM) and Scanning Electron Microscopy (SEM), Nature and Science, (2006) 14.

[49] B.H. Stuart, Infrared Spectroscopy: Fundamentals and Applications/H. Barbara Stuart, in, Wiley, 2004, 224 p.

[50] L.-E. Åmand, C.J. Tullin, The Theory Behind FTIR analysis, Department of Energy Conversion Chalmers University of Technology, Göteborg, Sweden, (1997).

[51] J. McCann, S. Badwal, Equivalent circuit analysis of the impedance response of semiconductor/electrolyte/counterelectrode cells, Journal of The Electrochemical Society, 129 (1982) 551-559.

[52] B. Igarashi, T. Christensen, E.H. Larsen, N.B. Olsen, I.H. Pedersen, T. Rasmussen, J.C. Dyre, An impedance-measurement setup optimized for measuring relaxations of glass-forming liquids, Review of Scientific Instruments, 79 (2008) 045106.

[53] E. Barsoukov, J.R. Macdonald, Impedance spectroscopy: theory, experiment, and applications, John Wiley & Sons, 2005.

[54] H. Fricke, XXXIII. The theory of electrolytic polarization, The London, Edinburgh, and Dublin Philosophical Magazine and Journal of Science, 14 (1932) 310-318.

[55] N.G. McCrum, B.E. Read, G. Williams, Anelastic and dielectric effects in polymeric solids, (1967).

[56] J. Ross, Macdonald, Impedance Spectroscopy, in, Wiley, New York, 1987.

[57] B. Dodrill, L.S. Cryotronics, Magnetic Media Measurements with a VSM, Lake Shore cryotronics, Inc, 575 (2009).

[58] P. Xu, X. Han, M. Wang, Synthesis and magnetic properties of BaFe12O19 hexaferrite nanoparticles by a reverse microemulsion technique, The Journal of Physical Chemistry C, 111 (2007) 5866-5870.

[59] S. Hussain, A. Maqsood, Influence of sintering time on structural, magnetic and electrical properties of Si–Ca added Sr-hexa ferrites, Journal of magnetism and magnetic materials, 316 (2007) 73-80.

[60] Y. Goto, T. Takada, Phase Diagram of the System BaO-Fe2O3, Journal of the American Ceramic Society, 43 (1960) 150-153.

[61] M. Erchak Jr, I. Fankuchen, R. Ward, Reaction between Ferric Oxide and Barium Carbonate in the Solid Phase. Identification of Phases by X-Ray Diffraction1, Journal of the American Chemical Society, 68 (1946) 2085-2093.

[62] M.J. Iqbal, M.N. Ashiq, Physical and electrical properties of Zr–Cu substituted strontium hexaferrite nanoparticles synthesized by co-precipitation method, Chemical Engineering Journal, 136 (2008) 383-389.

[63] P. Ayyub, Finite Size Effects in Ferroelectric Nanomaterials and Thin Films, PROCEEDINGS-INDIAN NATIONAL SCIENCE ACADEMY PART A, 67 (2001) 71-84.

[64] V.R. Mudinepalli, L. Feng, W.-C. Lin, B. Murty, Effect of grain size on dielectric and ferroelectric properties of nanostructured Ba0. 8Sr0. 2TiO3 ceramics, Journal of Advanced Ceramics, 4 (2015) 46-53.

[65] R.J. Pandya, U. Joshi, O. Caltun, Microstructural and Electrical Properties of Barium Strontium Titanate and Nickel Zinc Ferrite Composites, Procedia Materials Science, 10 (2015) 168-175.

[66] L. Kong, Z. Li, G. Lin, Y. Gan, Magneto-Dielectric Properties of Mg–Cu–Co Ferrite Ceramics: II. Electrical, Dielectric, and Magnetic Properties, Journal of the American Ceramic Society, 90 (2007) 2104-2112.

[67] I. Ali, M. Islam, N. Karamat, A. Iftikhar, A. Shah, M. Athar, I. Shakir, M.N. Ashiq, Synthesis and magnetic properties of (Eu–Ni) substituted Y-type hexaferrite by surfactant assisted co-precipitation method, Journal of Magnetism and Magnetic Materials, 385 (2015) 386-393.

[68] M. Ahmad, M. Rafiq, M. Hasan, Transport characteristics and colossal dielectric response of cadmium sulfide nanoparticles, Journal of Applied Physics, 114 (2013) 133702.

[69] V.N. Dhage, M. Mane, A. Keche, C. Birajdar, K. Jadhav, Structural and magnetic behaviour of aluminium doped barium hexaferrite nanoparticles synthesized by solution combustion technique, Physica B: Condensed Matter, 406 (2011) 789-793.

[70] P. Brito, R. Gomes, J. Duque, M. Macedo, SrFe 12 O 19 prepared by the proteic sol–gel process, Physica B: Condensed Matter, 384 (2006) 91-93.